Backbone curves, Neimark-Sacker boundaries and appearance of quasi-periodicity in nonlinear oscillators: application to 1:2 internal resonance and frequency combs in MEMS

Giorgio Gobat · **Louis Guillot** · **Attilio Frangi** · **Bruno Cochelin** ·
Cyril Touzé

Abstract Quasi-periodic solutions can arise in assemblies of nonlinear oscillators as a consequence of Neimark-Sacker bifurcations. In this work, the appearance of Neimark-Sacker bifurcations is investigated analytically and numerically in the specific case of a system of two coupled oscillators featuring a 1:2 internal resonance. More specifically, the locus of Neimark-Sacker points is analytically derived and its evolution with respect to the system parameters is highlighted. The backbone curves, solution of the conservative system, are first investigated, showing in particular the existence of two families of periodic orbits, denoted as parabolic modes. The behaviour of these modes, when the detuning between the eigenfrequencies of the system is varied, is underlined. The non-vanishing limit value, at the origin of one solution family, allows explaining the appearance of isolated solutions for the damped-forced system. The results are then applied to a Micro-Electro-Mechanical System-like shallow arch structure, to show how the analytical expression of the Neimark-Sacker boundary curve can be used for rapid prediction of the appearance of quasiperiodic regime, and thus frequency combs, in Micro-Electro-Mechanical System dynamics.

Abbreviations

FEM	Finite Element Method
FRF	Frequency Response Function
FT	Fourier Transform
FC	Frequency Comb
HB	Harmonic Balance
IR	Internal Resonance
MEMS	Micro-Electro-Mechanical systems
MS	Multiple Scales
NS	Neimark-Sacker
QP	Quasi-Periodic
ROM	Reduced Order Model
RK4	Runge-Kutta 4th Order

G. Gobat (✉) · A. Frangi
Politecnico di Milano, Piazza Leonardo da Vinci, 32, 20133 Milano, MI, Italy
e-mail: giorgio.gobat@polimi.it

L. Guillot · B. Cochelin
Laboratoire de Mécanique et d'Acoustique LMA - UMR 7031 AMU - CNRS - Centrale Marseille, 4 impasse Nikola Tesla CS 40006, 13453 Marseille Cedex 13, France

C. Touzé
Institute of Mechanical Sciences and Industrial Applications Institut Polytechnique de Paris CNRS - ENSTA Paris - EDF - CEA, 828 boulevard des Maréchaux, 91762 Palaiseau Cedex, France

1 Introduction

Nonlinear dynamical phenomena in mechanical systems are often connected with the description of complex features that have no counterpart in linear theory, like jump phenomena, hysteresis, quasiperiodicity and chaotic vibrations [18, 39, 54]. In recent years, a number of studies appeared in several fields of Physics and Mechanics, highlighting the occurrence of *Frequency Comb* (FC) in the observed dynamical responses, especially when the system is driven by a single harmonic component. In the frequency domain a FC is characterized by a collection of spectral lines of frequency $m\Omega \pm n\omega_{NS}$, where m and n are integers, Ω is the driving frequency and ω_{NS} is a new incommensurate frequency. In the time domain a FC is associated with a signal showing both amplitude and frequency modulation.

FCs have been largely investigated in optics where they have important applications in metrology, see *e.g.* [10, 29, 60, 63]. A strong link also exists with the so-called *modulation instability* studied in the physics of nonlinear waves [9, 64].

In recent years several occurrences of FCs have been documented in *Micro Electro-Mechanical Systems* (MEMS). These devices display a wide range of complex nonlinear phenomena, mainly due to their large quality factors Q, typically ranging from 10^3 to 10^6. Indeed MEMS are often monolithic structures encapsulated in near vacuum packages and their dissipation is drastically reduced with respect to macrostructures. *Internal resonance* (IR) plays an important role in triggering more complex motions and facilitate energy transfer between modes and also the onset of quasiperiodicity [1, 2, 6, 22, 23, 44, 58, 59]. Indeed in most cases, FCs in MEMS are associated with IR phenomena. FCs have been experimentally observed in [7, 8] addressing a MEMS resonator with strong 1:3 IR between bending and torsional modes. Another example is provided in [31], where a resonator is proposed in which the dissipation can be dynamically eliminated, leading to the appearance of a tunable FC. In [45] the formation, evolution, and tuning of FCs in a piezoelectric MEMS resonator, based on nondegenerate parametric pumping, is presented. The tuning mechanisms of FCs are discussed with specific attention to the dependence of the center frequency and the frequency spacing between

the spectral lines on the external input. In [22] a 1:2 IR between the first two symmetric vibrational modes of a MEMS arch resonator is investigated experimentally and theoretically. The MEMS structure is electro-thermally tuned and electro-statically driven. Here FCs are observed amid a variety of other complex behaviours. Other noteworthy studies on IR in MEMS arch resonators, with experimental data supported by theoretical models, can be found in [46, 47]. In the context of MEMS piezoresonators, similar phenomena have been demonstrated in [14–16]. In particular, if the system has two modes with eigenfrequencies f_1 and f_2 such that $f_2 \approx f_1/2$, an excitation can activate parametric resonance and trigger a FC. However, it is worth mentioning that FCs in MEMS might be associated with different phenomena. An example is discussed in [19] where FCs arise as a consequence of intermittent contact between deformable beams in a MEMS structure.

The issue of predicting the onset of a FC is strongly linked to the stability analysis of the associated periodic response. Once it gets unstable, a *Quasi-Periodic* (QP) regime might arise thus creating a FC. Restraining ourselves to the case of nonlinear vibrations, this problem can be reformulated as finding the locus of bifurcation points in periodic responses originating quasi-periodicity. In most cases these can be classified as *Neimark-Sacker* (NS) bifurcations [41, 48], which represent the main focus of this work. It is however worth stressing that the onset of QP solutions and FCs have been also observed in [7, 8] as a consequence of a Saddle-Node-Invariant-Circle (SNIC) bifurcation [51]. Besides, the stability of QP solutions developing on a torus is a fundamental aspect for questioning the appearance of chaos related to the stability of the period-three solutions [3, 4, 21, 28, 42].

The appearance of NS bifurcations in systems with IR has already been reported for systems featuring 1:1 IR, see *e.g.* [56] for arches or [57] for circular cylindrical shells, as well as for systems with 1:2 IR [39, 40, 54] such as arches [55]. Other examples involve different physical phenomena like, for instance, the aero-elastic behaviour of a flexible elastic suspended cable with linear eigenfrequencies in an almost 1:2 ratio driven by the wind speed [30]. Finally, NS bifurcations can also originate in more

complex 1:2:2 and 1:2:4 resonance scenarios as reported in [36].

One can also remark that the computation of the locus of specific bifurcation points, as parameters are varied, has recently stimulated intensive research also on numerical techniques. For instance, continuation methods can be suitably adapted with additional constraints to follow the evolution of a given bifurcation point in the parameter space [11, 61, 62].

This work focuses on the appearance of QP solutions in nonlinear oscillators featuring 1:2 internal resonance. In this context NS bifurcation points have been known for a long time, see e.g. [35, 37, 38, 40] and references therein. Consequently the viewpoint of the present contribution is to revisit a classical example in nonlinear oscillations, bring new results and use them in the perspective of better understanding and predicting the occurrence of frequency combs in MEMS dynamics. The main outcomes of the present study are to derive an analytical formula for the locus of NS boundaries, exhibit the two different families of periodic solutions connected to the two backbone curves of the system, named them as parabolic modes, and clearly highlight the links between the backbones, the frequency-response curves, the existence of isolated solutions and the locus of NS points. Since applications to MEMS-like structure are targeted, an arch structure is used in order to show how the findings can be used for fast prediction of the onset of FC in MEMS dynamical solutions.

The formulas derived analytically give simplified models that can be applied in systems that admit order reduction. In this work we consider systems in which it is possible to apply the center manifold theorem and more generally invariant and inertial manifold theory (see [24, 33, 34, 52]). In this framework, strong but reliable simplifications can be applied and even continuous systems may be reduced to a limited number of degrees of freedom.

Future investigations will address the cases of 1:1 and 1:3 IRs, framing all these systems within the same setting and offering a unified view on the appearance of quasiperiodicity and link to backbones in assemblies of nonlinear oscillators featuring IR.

The paper is organized as follows. Sect. 2 is devoted to the analysis of conservative systems with the multiple scales technique. Two families of parabolic modes are identified and associated with two different backbone curves. The behaviour of these families of solution, for system parameters variation, is investigated. Sect. 3 is concerned with the analysis of the forced-damped system. A connection with the limit values of the conservative solution is given, and the appearance of isolas is explained. The NS boundary curve is computed and its dependence upon parameters and shape variation is analysed in detail.

Finally, in Sect. 4, a MEMS-like arch structure is analysed and the analytical expression of NS boundary curves is utilized to predict the occurrence of QP solutions, which represents the primary goal of the paper. Reduced order models using implicit static condensation [13, 25, 50] are obtained starting from the Finite Element (FE) discretization. The dynamics of the system is studied numerically through harmonic balance and direct time integration techniques in order to validate and refine the analytical estimate.

2 Conservative system: backbone curves

Let us consider the normal form of a system of two coupled nonlinear oscillators featuring 1:2 IR:

$$\ddot{q}_1 + \omega_1^2 q_1 + 2\mu_1 \dot{q}_1 + \alpha_{12} q_1 q_2 = F\cos(\Omega t), \qquad (1a)$$

$$\ddot{q}_2 + \omega_2^2 q_2 + 2\mu_2 \dot{q}_2 + \alpha_{11} q_1^2 = 0, \qquad (1b)$$

in which q_i, $(i = 1, 2)$ denote the displacement of each oscillator, ω_i the eigenfrequencies, α_{12}, α_{11} the nonlinear positive quadratic coupling coefficients, μ_i, $(i = 1, 2)$ the linear damping coefficients and Ω the angular frequency of the forcing term with intensity F. Since we are interested in the 1:2 IR, the eigenfrequencies are such that $\omega_2 \approx 2\omega_1$. In a conservative context, where internal forces derive from a potential, we have $\alpha_{11} = \alpha_{12}/2$. However, since the results discussed in what follows can be used in more general contexts such as e.g. economy, chemistry or biology, in Appendix 1 we will relax this assumption and show examples of the behaviour for more general cases of quadratic coupling coefficients.

In this section, we address conservative dynamics and discard consequently the damping and forcing terms from the equations of motion. We apply the method of Multiple Scales (MS) to system (1) following [40]. Only the main results are recalled with emphasis on new findings. The detailed MS

procedure is given in Appendix 2 for the sake of completeness.

2.1 Multiple scales solution

The method of MS expresses the solution as a composition of different time scales $T_j = \varepsilon^j t$ for $j = 0, 1$, and decomposes the solution as $q_i(t) = q_{i0}(T_0, T_1) + \varepsilon q_{i1}(T_0, T_1) + O(\varepsilon^2)$ with $i = 1, 2$ and ε a small bookkeeping parameter. We also assume that the nonlinear coefficients are small and can be expressed as $\alpha_{12} = \varepsilon \bar{\alpha}_{12}$ and $\alpha_{11} = \varepsilon \bar{\alpha}_{11}$. Starting from Eq. (1) and introducing the MS expansions, we sort non-linearities according to ε and we ignore the forcing F and the damping terms μ_i (see details in Appendix 2). The closeness of the fulfilment of the 1:2 ratio between the eigenfrequencies is quantified by introducing an internal detuning parameter σ_1 such that

$$\omega_2 = 2\omega_1 + \varepsilon\sigma_1. \tag{2}$$

We introduce a polar form for $q_{10}(t)$

$$q_{10}(t) = \frac{a_1(T_1)}{2} \exp(\mathbb{i}\theta_1(T_1) + \mathbb{i}\omega_1 T_0) + c.c., \tag{3a}$$

$$q_{20}(t) = \frac{a_2(T_1)}{2} \exp(\mathbb{i}\theta_2(T_1) + \mathbb{i}\omega_2 T_0) + c.c., \tag{3b}$$

where $c.c.$ stands for complex conjugate; $a_1(T_1)$, $a_2(T_1)$ are unknown amplitudes; $\theta_1(T_1)$, $\theta_2(T_1)$ are unknown phases, varying at the slow time scale T_1 and $\mathbb{i}$ is the imaginary unit. Developing the solvability condition (see details given in Appendix 2), we arrive at the modulation equations for amplitudes and phases:

$$a_1' = \frac{\bar{\alpha}_{12} a_1 a_2 \sin(2\theta_1 - \theta_2 - \sigma_1 T_1)}{4\omega_1}, \tag{4a}$$

$$a_1 \theta_1' = \frac{\bar{\alpha}_{12} a_1 a_2 \cos(2\theta_1 - \theta_2 - \sigma_1 T_1)}{4\omega_1}, \tag{4b}$$

$$a_2' = -\frac{\bar{\alpha}_{11} a_1^2 \sin(2\theta_1 - \theta_2 - \sigma_1 T_1)}{4\omega_2}, \tag{4c}$$

$$a_2 \theta_2' = \frac{\bar{\alpha}_{11} a_1^2 \cos(2\theta_1 - \theta_2 - \sigma_1 T_1)}{4\omega_2}. \tag{4d}$$

Inspecting Eq. (4), three different classes of possible solutions can be identified: 1) uncoupled solution

with $a_1 \neq 0$ and $a_2 = 0$, denoted A1-mode in what follows; 2) uncoupled solution with $a_2 \neq 0$ and $a_1 = 0$, denoted A2-mode; 3) coupled solutions with both $a_2 \neq 0$ and $a_1 \neq 0$. The A1-mode is not admissible because of the invariant-breaking term $\alpha_{11} q_1^2$ in Eq. (1) considering the conservative condition. Indeed inserting $q_2 = 0$ in Eq. (1b) implies that also $q_1 = 0$. The A2-mode is admissible, since inserting $q_1 = 0$ Eq. (1b) reduces to a linear oscillator, while Eq. (1a) is trivially satisfied.

Considering now the coupled solutions with both a_1 and a_2 different from zero, we simplify Eq. (4), dividing by the non-zero amplitudes a_1 and a_2:

$$a_1' = \frac{\bar{\alpha}_{12} a_1 a_2 \sin(2\theta_1 - \theta_2 - \sigma_1 T_1)}{4\omega_1}, \tag{5a}$$

$$\theta_1' = \frac{\bar{\alpha}_{12} a_2 \cos(2\theta_1 - \theta_2 - \sigma_1 T_1)}{4\omega_1}, \tag{5b}$$

$$a_2' = -\frac{\bar{\alpha}_{11} a_1^2 \sin(2\theta_1 - \theta_2 - \sigma_1 T_1)}{4\omega_2}, \tag{5c}$$

$$\theta_2' = \frac{\bar{\alpha}_{11} a_1^2 \cos(2\theta_1 - \theta_2 - \sigma_1 T_1)}{4 a_2 \omega_2}. \tag{5d}$$

To analyse the permanent solutions corresponding to fixed points of Eq. (5), the system needs to be made autonomous. We observe that the phases appearing in the sine and cosine functions involve the same quantity $2\theta_1 - \theta_2 - \sigma_1 T_1$. This means that the system can be made autonomous with only two amplitudes and one phase. However, if one adopts such a choice an indeterminate quantity will appear when reconstructing the whole solutions for q_1 and q_2, since both θ_1 and θ_2 will need to have an initial phase. To solve this issue, it has been preferred to make the system autonomous using two angular variables.

$$\gamma_1 = \theta_1, \tag{6a}$$

$$\gamma_p = 2\theta_1 - \sigma_1 T_1 - \theta_2. \tag{6b}$$

The resulting autonomous system reads

$$a_1' = \frac{\bar{\alpha}_{12} a_1 a_2 \sin(\gamma_p)}{4\omega_1}, \tag{7a}$$

$$\gamma_1' = \frac{\bar{\alpha}_{12} a_2 \cos(\gamma_p)}{4\omega_1}, \tag{7b}$$

$$a_2' = -\frac{\bar{\alpha}_{11} a_1^2 \sin(\gamma_p)}{4\omega_2}, \tag{7c}$$

$$\gamma_p' = -\frac{\bar{\alpha}_{11} a_1^2 \cos(\gamma_p)}{4a_2\omega_2} - \sigma_1 + \frac{\bar{\alpha}_{12} a_2 \cos(\gamma_p)}{2\omega_1}. \tag{7d}$$

Obviously, Eq. (7b) is redundant since only γ_p appears elsewhere in the system.

2.2 Coupled solutions: parabolic modes and backbone curves

The fixed point solutions of Eq. (7) exist only when $\sin(\gamma_p) = 0$ and consequently $\cos(\gamma_p) = \pm 1 = p$, where the notation $p = \pm 1$ is introduced for the rest of the paper. Consequently, the only possible coupled solutions correspond to limit cycles with a_1 and a_2 constants independent of time T_1.

The strong constraints imposed on the angular variables define two classes of solutions: one related to $p = 1$ and one to $p = -1$. We will show in the following that each of these solutions is associated to a family of periodic orbits with a given amplitude-frequency relationship (or backbone curve). To better describe the typology of these two solutions, let us first reconstruct the first order amplitudes q_{10} and q_{20}. Combining Eq. (3) with Eq. (6), the first order solutions are obtained as

$$q_{10}(t) = a_1 \cos(\gamma_1 + \omega_1 t), \tag{8a}$$

$$q_{20}(t) = a_2 \cos(2(\gamma_1 + \omega_1 t) - \gamma_p). \tag{8b}$$

When $p = +1$, then $\gamma_p = 2m\pi$ with m integer and the following relationship between the amplitudes holds:

$$2\frac{q_{10}^2}{a_1^2} - 1 = \frac{q_{20}}{a_2}. \tag{9}$$

Eq. (9) dictates that the amplitudes lie on a parabola with positive concavity in the configuration plane (q_{10}, q_{20}). In the whole four-dimensional phase space (including both velocities), we hence obtain a family of periodic orbits developing on a manifold such that its projection on (q_{10}, q_{20}) is a parabola. This solution is called parabolic mode, following also the

designation given in [6, 17, 32] for the case of 1:1 resonance, where normal modes and elliptic modes are the two families of coupled solutions. More precisely, in the case $p = +1$, this solution is denoted as p^+-mode.

When $p = -1$ a second family of periodic orbit is obtained, where $\gamma_p = (2m+1)\pi$, with m integer. The amplitudes now define a parabola with negative concavity in the configuration plane (q_{10}, q_{20}):

$$-2\frac{q_{10}^2}{a_1^2} + 1 = \frac{q_{20}}{a_2}, \tag{10}$$

denoted as p^--mode . These two families of solutions are represented in Fig. 1. It should be noted that for the p^+-mode q_1 and q_2 have the same phase, while for the p^--mode the phase difference is equal to π.

In order to express the frequency-amplitude relationship (backbone curves) for these two families of coupled solutions, we elaborate on the relationship between the amplitudes a_1 and a_2 given by the fixed point equation associated to Eq. (7d):

$$\varepsilon\left(\frac{\bar{\alpha}_{11} a_1^2 p}{4a_2\omega_2} + \frac{\bar{\alpha}_{12} a_2 p}{2\omega_1}\right) + \omega_2 - 2\omega_1 = 0, \tag{11}$$

where we have replaced the detuning variable σ_1 with its expression in terms of eigenfrequencies $\omega_{1,2}$ to have a more straightforward insight into the system. Denoting with $\bar{q}_i$ the maximum amplitude of $q_i(t)$ ($\bar{q}_i = a_i, i = 1, 2$), we now replace the non-linear coefficients with the original α_{12} and α_{11}, and we express $\bar{q}_1$ in terms of $\bar{q}_2$:

$$\bar{q}_1^2 = \left(\frac{2\bar{q}_2\alpha_{12}}{\omega_1} - \frac{4(\omega_2 - 2\omega_1)}{p}\right)\frac{\bar{q}_2\omega_2}{\alpha_{11}}. \tag{12}$$
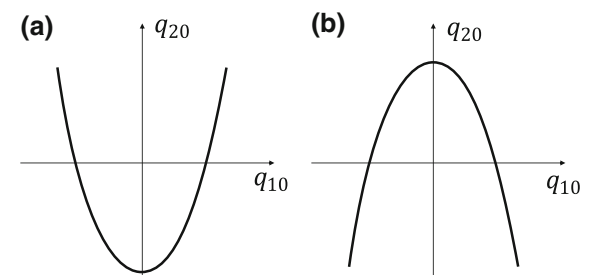
which holds for both parabolic modes, setting either

Fig. 1 Sketch of the parabolic modes corresponding to the coupled solutions in the configuration plane (q_{10}, q_{20}). a) p^+-mode, b) p^--mode

$p = 1$ or $p = -1$. To obtain the amplitude-frequency relationship we first solve the first-order equations at the slow time scale T_1, Eq. (7), and get the following expressions for the phase angles:

$$\gamma_1 = \frac{\bar{\alpha}_{12} a_2 p}{4\omega_1} T_1 + \phi_1, \tag{13a}$$

$$\gamma_p = -\frac{\bar{\alpha}_{11} a_1^2 p}{4 a_2 \omega_2} T_1 - \frac{(\omega_2 - 2\omega_1)}{\varepsilon} T_1 - \frac{\bar{\alpha}_{12} a_2 p}{2\omega_1} T_1 + \phi_p, \tag{13b}$$

with ϕ_1 and ϕ_p integration constants. Using Eq. (6), the original nonlinear coefficients α_{12} and α_{11} and using $T_1 = \varepsilon t$ we have:

$$\theta_1 = \frac{\alpha_{12} a_2 p}{4\omega_1} t + \phi_1, \tag{14a}$$

$$\theta_2 = \frac{\alpha_{11} a_1^2 p}{4 a_2 \omega_2} t + 2\phi_1 - \phi_p, \tag{14b}$$

Inserting these equations in Eq. (3) we get

$$q_{10}(t) = a_1 \cos\left(\frac{\alpha_{12} a_2 p}{4\omega_1} t + \omega_1 t + \phi_1\right), \tag{15a}$$

$$q_{20}(t) = a_2 \cos\left(a_1^2 \frac{p}{4} \frac{\alpha_{11}}{a_2 \omega_2} t + \omega_2 t + 2\phi_1 - \phi_p\right). \tag{15b}$$

From Eq. (15), substituting $\bar{q}_{1,2}$, one obtains the nonlinear oscillation frequencies $\omega_{\mathrm{NL}i}$ of each oscillator:

$$\omega_{\mathrm{NL}1} = \omega_1 + \frac{\alpha_{12} \bar{q}_2 p}{4\omega_1}, \tag{16a}$$

$$\omega_{\mathrm{NL}2} = \omega_2 + \bar{q}_1^2 \frac{p}{4} \frac{\alpha_{11}}{\bar{q}_2 \omega_2}. \tag{16b}$$

We remark in particular that the relationship $\omega_{\mathrm{NL}2} = 2\omega_{\mathrm{NL}1}$ is always fulfilled, as can be shown inserting Eq. (12) into Eq. (16b).

For the sake of clarity, $\omega_{\mathrm{NL}1}$ will be simply denoted ω_{NL} in what follows. Note that Eq. (16a), together with Eq. (12), identifies the solution manifold in the space $(\omega_{\mathrm{NL}}, \bar{q}_1, \bar{q}_2)$ where the backbone solutions are lying. The two families of solutions are discriminated by replacing p with ± 1 in all expressions. Since the amplitudes $\bar{q}_1$, $\bar{q}_2$ are assumed to be positive, one arrives at the conclusion that: when $\omega_{\mathrm{NL}} < \omega_1$, only the p^- mode exists, while when $\omega_{\mathrm{NL}} > \omega_1$, one only has

the p^+-mode. This gives a first condition for the existence of the backbone curves.

An additional condition can be derived by inserting Eq. (16a) in the rhs of Eq. (12) that must be positive to guarantee the existence of a solution for $\bar{q}_1$:

$$(-2\omega_{\mathrm{NL}} + \omega_2)(\omega_1 - \omega_{\mathrm{NL}})\left(\frac{16\omega_1 \omega_2}{\alpha_{12} \alpha_{11} p^2}\right) > 0. \tag{17}$$

In Eq. (17), the third term is always positive due to the assumptions on α_{12}. The first two factors of Eq. (17) impose that $\bar{q}_1$ exists only for values of ω_{NL} outside the limit points $\omega_{\mathrm{NL}} = \omega_1$ and $\omega_{\mathrm{NL}} = \omega_2/2$.

The existence regions of each parabolic modes are summarized in Fig. 2 in terms of the shift of the nonlinear oscillation frequency $\omega_{\mathrm{NL}} - \omega_1$ (on the x-axis) and of the detuning $\omega_2 - 2\omega_1$ (on the y-axis). For a given system, the detuning is fixed so that a single horizontal line gives the existence region. The blue region (respectively the red region) corresponds to the existence of p^- (resp. p^+) mode. From Eq. (17), the lines $\omega_{\mathrm{NL}} = \omega_2/2$ (highlighted with a green color) and the y-axis $\omega_{\mathrm{NL}} = \omega_1$, delimit a region in which no coupled solutions exist. The green hatched region delimited by $\omega_{\mathrm{NL}} = \omega_2/2$ and $\omega_{\mathrm{NL}} = \omega_2/6 + 2\omega_1/3$ is commented in Sect. 2.3.

It is worth looking at the behaviour of the backbones at the limit point of their existence regions. At the first boundary $\omega_{\mathrm{NL}} = \omega_1$ we get:
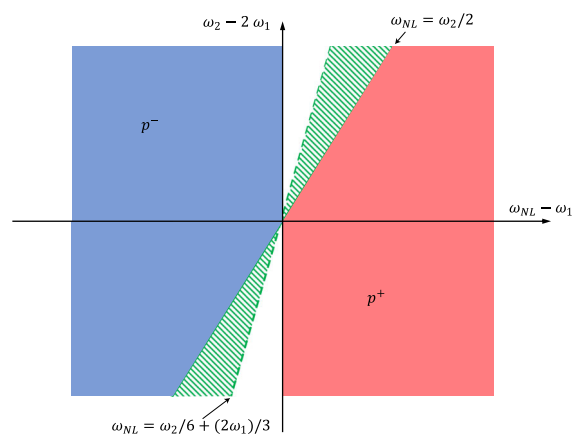

Fig. 2 Schematic representation of the existence region for the coupled parabolic modes, in the plane $(\omega_{\mathrm{NL}} - \omega_1, \omega_2 - 2\omega_1)$. The abscissa represents the shifted nonlinear oscillation frequency while the ordinate is the detuning between the eigenfrequencies of the system

$$\lim_{\omega_{NL} \to \omega_1} \bar{q}_1 = 0, \qquad \lim_{\omega_{NL} \to \omega_1} \bar{q}_2 = 0, \tag{18}$$

meaning that close to ω_1, the backbone curve amplitudes are going to zero as expected. The situation is different in the vicinity of $\omega_2/2$. Indeed at this second boundary $\omega_{NL} = \omega_2/2$, one obtains:

$$\lim_{\omega_{NL} \to \omega_2/2} \bar{q}_1 = 0, \tag{19a}$$

$$\lim_{\omega_{NL} \to \omega_2/2} \bar{q}_2 = \frac{2\omega_1(\omega_2 - 2\omega_1)}{\alpha_{12}p}. \tag{19b}$$

In particular the limit value of $\bar{q}_2$ is non-zero at the limit point of the backbone when $\omega_{NL} \longrightarrow \omega_2/2$, which could appear conflicting with the coupled solution assumptions. One should note that this is only true in the limit, and that the uncoupled A2-mode solution still exists for the system. Consequently the limit point of the backbone connects with this solution at this specific point. This particular situation induces a jump in the backbone solution (see the detuned condition in Fig. 3 commented in Sect. 2.4) and, as

shown in Sect. 3.2, will also lead to the emergence of isolated solutions in the forced and damped system.

2.3 Stability of coupled solutions

The stability of coupled solutions is governed by the eigenvalues of the Jacobian matrix J of the conservative system (see Appendix 2 for details). The determinant $\det(\lambda I - J)$ of the characteristic polynomial, expressing the angular variables in terms of $\bar{q}_i, i = 1, 2$, writes:

$$\det(\lambda I - J) = \frac{\lambda^2}{16\bar{q}_2^2 \omega_1 \omega_2^2} \left(4\alpha_{12}\alpha_{11}p^2 \bar{q}_1^2 \bar{q}_2^2 \omega_2 \right. \tag{20}$$
$$\left. + \omega_1 \left(\alpha_{11}^2 p^2 \bar{q}_1^4 + 16\lambda^2 \bar{q}_2^2 \omega_2^2 \right) \right).$$

The nonzero eigenvalues λ are given by:

$$\lambda = \pm\sqrt{(6\omega_{NL} - 4\omega_1 - \omega_2)(\omega_2 - 2\omega_{NL})}. \tag{21}$$
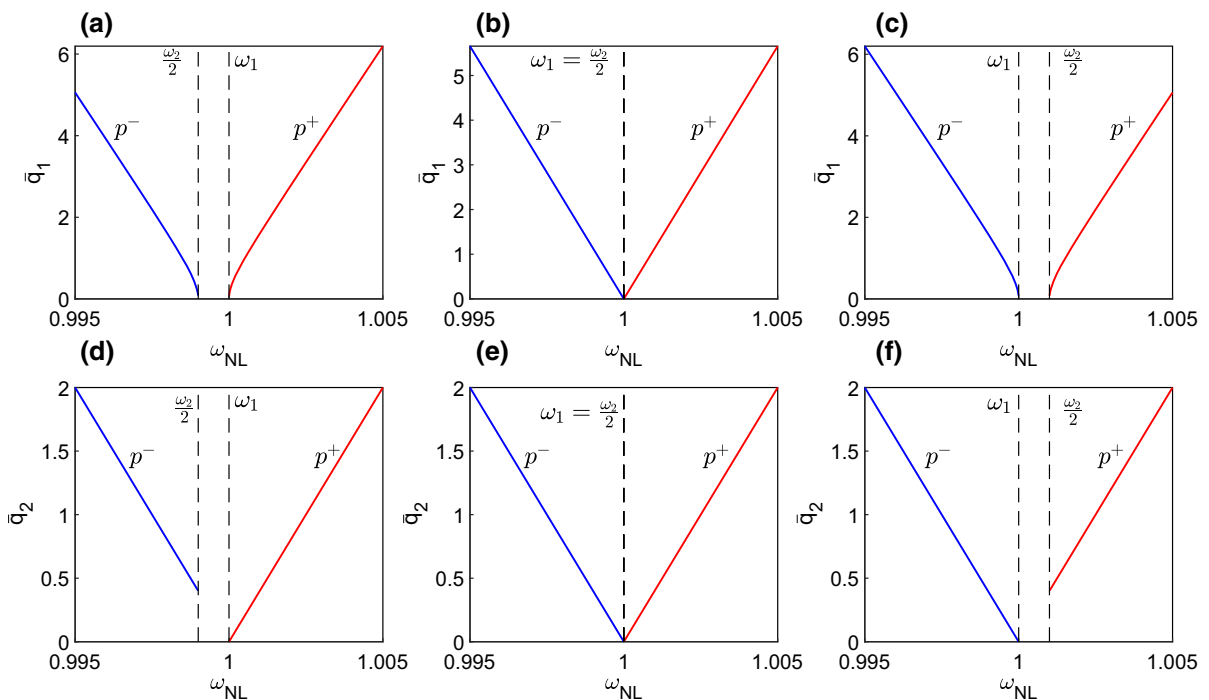
and have negative real part if:

Fig. 3 Backbone curves of the two families p^+ (red curves) and p^--modes (blue curves), in the plane (ω_{NL}, a_1) (first row) and (ω_{NL}, a_2) (second row), and for three different possible cases. First column: $\omega_2/2 < \omega_1$, second column: $\omega_2/2 = \omega_1$, third column: $\omega_2/2 > \omega_1$. In the figure, $\omega_1 = 1$, $\alpha_{12} = 1 \cdot 10^{-2}$, $\alpha_{11} = 5 \cdot 10^{-3}$

$$\omega_{\text{NL}} < \frac{2\omega_1}{3} + \frac{\omega_2}{6} \quad \text{and} \quad \omega_{\text{NL}} > \frac{\omega_2}{2}. \tag{22}$$

The unstable region delimited by conditions in Eq. (22) is shown in Fig. 2 as the green hatched region. We observe that this region completely falls in a non-existence area of coupled solutions. Consequently, the conservative backbone curves are always stable.

2.4 Backbone curves

In this section, we show how the backbone curves of the two different parabolic modes organize when the detuning parameter is varied. Note that some of the results presented here are close to those presented in [27], where a different point of view was adopted on the same system. Fig. 3 shows the three different possible cases: when the detuning is negative, when it is vanishing, and when it is positive. The figure plots the projection of the solutions in the planes $(\omega_{\text{NL}}, \bar{q}_1)$ and $(\omega_{\text{NL}}, \bar{q}_2)$. However, an optimal representation would be in the 3D space $(\omega_{\text{NL}}, \bar{q}_1, \bar{q}_2)$, as will be shown in Sect. 3 when the solutions will be fully reconstructed.

One can note that, consistently with Eq. (12)-(16), the backbones in the $(\omega_{\text{NL}}, \bar{q}_2)$ plane are always straight lines, while their projection in the $(\omega_{\text{NL}}, \bar{q}_1)$ plane are line segments only when the detuning vanishes, and otherwise have a parabolic shape. While increasing the detuning from negative to positive, one can observe the following features. When $\omega_2/2 < \omega_1$, the backbone starting at ω_1 is a p^+-mode, while the backbone starting at $\omega_2/2$ is a p^--mode. According to Eq. (19b), the p^--mode backbone starts from a nonzero value in $(\omega_{\text{NL}}, \bar{q}_2)$ plane. In the case of perfect 2:1 resonance, $\omega_2/2 = \omega_1$, the backbones of the two families start from the same point and from zero amplitude. Symmetrically, when $\omega_2/2 > \omega_1$, the backbone emanating from ω_1 is now a p^--mode, meaning that in the process of the transition a switch of family occurs. Consequently, the family of periodic solutions emanating from $\omega_2/2$ is now a p^+-mode, and it starts at a non-zero value in the $(\omega_{\text{NL}}, \bar{q}_2)$ plane.

3 Forced system and NS boundaries

This section investigates the Frequency Response Functions (FRF) of the oscillators described by Eq. (1), with a forcing term applied on the low-frequency oscillator and damping. While the appearance of quasi-periodic solutions has been already documented for this case *e.g.* in [40, 55], our aim here is to provide an exact expression of the NS boundary curve. Note also that quasiperiodic solutions are usually not addressed in the case where the forcing is applied on the high-frequency mode since the main concern is typically to investigate the loss of stability of the uncoupled solution [40, 53]. As for the conservative case, first-order perturbative solutions are derived with the MS method. Since this derivation is classical, most of the details are reported in Appendix 3, and emphasis is rather set on the derivation of the NS boundary curve, its dependence on parameters and the link between the FRF and the backbones.

3.1 Multiple Scales solution

First, the equations of motion in Eq. (1) are rewritten considering the MS expansion for time and oscillators degrees of freedoom using a bookkeeping parameter ε (see Appendix 3). We also introduce the assumptions that the non-linearities, the forcing amplitude and the damping are small, and can be expressed as $\alpha_{12} = \varepsilon\bar{\alpha}_{12}$, $\alpha_{11} = \varepsilon\bar{\alpha}_{11}$, $\mu_1 = \varepsilon\bar{\mu}_1$ and $F = \varepsilon\bar{F}$. The forcing angular frequency is in the vicinity of the first eigenfrequency ω_1, and an external detuning parameter σ_2 is introduced to describe this nearness as:

$$\Omega = \omega_1 + \varepsilon\sigma_2. \tag{23}$$

The first-order system governing the modulation of the amplitude is derived in a similar way as in the previous section. At the slow time scale T_1, the resulting system reads:

$$\begin{aligned} a_1' = &\frac{\bar{\alpha}_{12}a_1a_2 \sin(2\theta_1 - \theta_2 - \sigma_1 T_1)}{4\omega_1} \\ &- \frac{\bar{F}\sin(\theta_1 - \sigma_2 T_1)}{2\omega_1} - \bar{\mu}_1 a_1, \end{aligned} \tag{24a}$$

$$a_1\theta'_1 = \frac{\bar{\alpha}_{12}a_1a_2\cos(2\theta_1 - \theta_2 - \sigma_1 T_1)}{4\omega_1}$$
$$- \frac{\bar{F}\cos(\theta_1 - \sigma_2 T_1)}{2\omega_1}, \tag{24b}$$

$$a'_2 = -\frac{\bar{\alpha}_{11}a_1^2\sin(2\theta_1 - \theta_2 - \sigma_1 T_1)}{4\omega_2} - \bar{\mu}_2 a_2, \tag{24c}$$

$$a_2\theta'_2 = \frac{\bar{\alpha}_{11}a_1^2\cos(2\theta_1 - \theta_2 - \sigma_1 T_1)}{4\omega_2}. \tag{24d}$$

When the forcing is applied on the low-frequency oscillator, only coupled solutions exist (see Appendix 3).

The system is made autonomous by introducing γ_1 and γ_2 such that:

$$\gamma_1 = \theta_1 - T_1\sigma_2, \tag{25a}$$

$$\gamma_2 = 2\theta_1 - \sigma_1 T_1 - \theta_2, \tag{25b}$$

and reads:

$$a'_1 = \frac{a_1(\bar{\alpha}_{12}a_2\sin(\gamma_2) - 4\bar{\mu}_1\omega_1) - 2\bar{F}\sin(\gamma_1)}{4\omega_1}, \tag{26a}$$

$$\gamma'_1 = \frac{\bar{\alpha}_{12}a_1a_2\cos(\gamma_2) - 2\bar{F}\cos(\gamma_1)}{4a_1\omega_1} - \sigma_2, \tag{26b}$$

$$a'_2 = -\frac{\bar{\alpha}_{11}a_1^2\sin(\gamma_2)}{4\omega_2} - \bar{\mu}_2 a_2, \tag{26c}$$

$$\gamma'_2 = \frac{1}{2}\cos(\gamma_2)\left(\frac{\bar{\alpha}_{12}a_2}{\omega_1} - \frac{\bar{\alpha}_{11}a_1^2}{2a_2\omega_2}\right) - \frac{\bar{F}\cos(\gamma_1)}{a_1\omega_1} - \sigma_1. \tag{26d}$$

It is worth highlighting that the definitions of Eqs. (25) and (6) and the structure of Eqs. (26) and (7) are similar and only differ for the additional terms associated to $\bar{F}$, $\bar{\mu}_i$ and σ_2.

The fixed points, associated to forced oscillations of constant amplitudes, can be expressed as function of the maximum amplitudes of $(\bar{q}_1, \bar{q}_2)$ only. Internal and external detunings σ_1 and σ_2 can also be replaced by the frequency differences to have a more straightforward insight into the system. The amplitude equations, considering the original system parameters, reads:

$$\bar{q}_2^3 + \frac{8\omega_1\Gamma}{\alpha_{12}}((\Omega - \omega_1)(\omega_2 - 2\Omega) + \mu_1\mu_2)\bar{q}_2^2$$
$$+ \frac{16\omega_1^2}{\alpha_{12}^2}((\Omega - \omega_1)^2 + \mu_1^2)\bar{q}_2 - \frac{\Gamma\alpha_{11}F^2}{\alpha_{12}^2\omega_2} = 0, \tag{27a}$$

$$\bar{q}_1 = \sqrt{\frac{4\omega_2\bar{q}_2}{\alpha_{11}\Gamma}}, \tag{27b}$$

with $\Gamma = \sqrt{\frac{1}{\mu_2^2 + (\omega_2 - 2\Omega)^2}}$. Eq. (27b) can be seen as the solution manifold in the space $(\Omega, \bar{q}_1, \bar{q}_2)$.

Eq. (27a) is a polynomial of the third-order in $\bar{q}_2$ and can give, depending on the parameters, from one to three solutions. The phases of fixed points are given by:

$$\cos(\gamma_1) = \frac{\bar{q}_1}{2F}(\alpha_{12}\cos(\gamma_2)\bar{q}_2 + 4\omega_1(\omega_1 - \Omega)), \tag{28a}$$

$$\sin(\gamma_1) = \frac{\bar{q}_1}{2F}(\alpha_{12}\sin(\gamma_2)\bar{q}_2 - 4\mu_1\omega_1), \tag{28b}$$

$$\cos(\gamma_2) = \frac{4\bar{q}_2\omega_2(2\Omega - \omega_2)}{\alpha_{11}\bar{q}_1^2}, \tag{28c}$$

$$\sin(\gamma_2) = -\frac{4\mu_2\bar{q}_2\omega_2}{\alpha_{11}\bar{q}_1^2}. \tag{28d}$$

These equations are not strictly necessary to build FRFs, but are needed to reconstruct the amplitude variations in time. They can also be used to establish existence conditions for the solutions exploiting the bounds of the trigonometric functions.

Fig. 4 shows the type of solutions obtained when varying the frequency detuning and the link with the backbone curve and the p^+ or p^- modes. Note that in Fig. 4 emphasis is put on the shape of the solution, while stability is addressed in the following section.

In the first line, the case of a positive detuning between the eigenfrequencies is considered, $\omega_2/2 > \omega_1$. In particular one can observe that close to $\Omega = \omega_2/2$, the FRF has a local minimum for a_1 and a maximum for a_2. The resonant branches follow the backbones of the two families of periodic orbits p^+ and p^-. Fig. 4 c) depicts the solution in the configuration plane (q_1, q_2) for the three points marked with coloured circles on the FRF. As expected, the blue point corresponds to p^--mode and one recovers the shape of the parabola in (q_1, q_2), with a slight
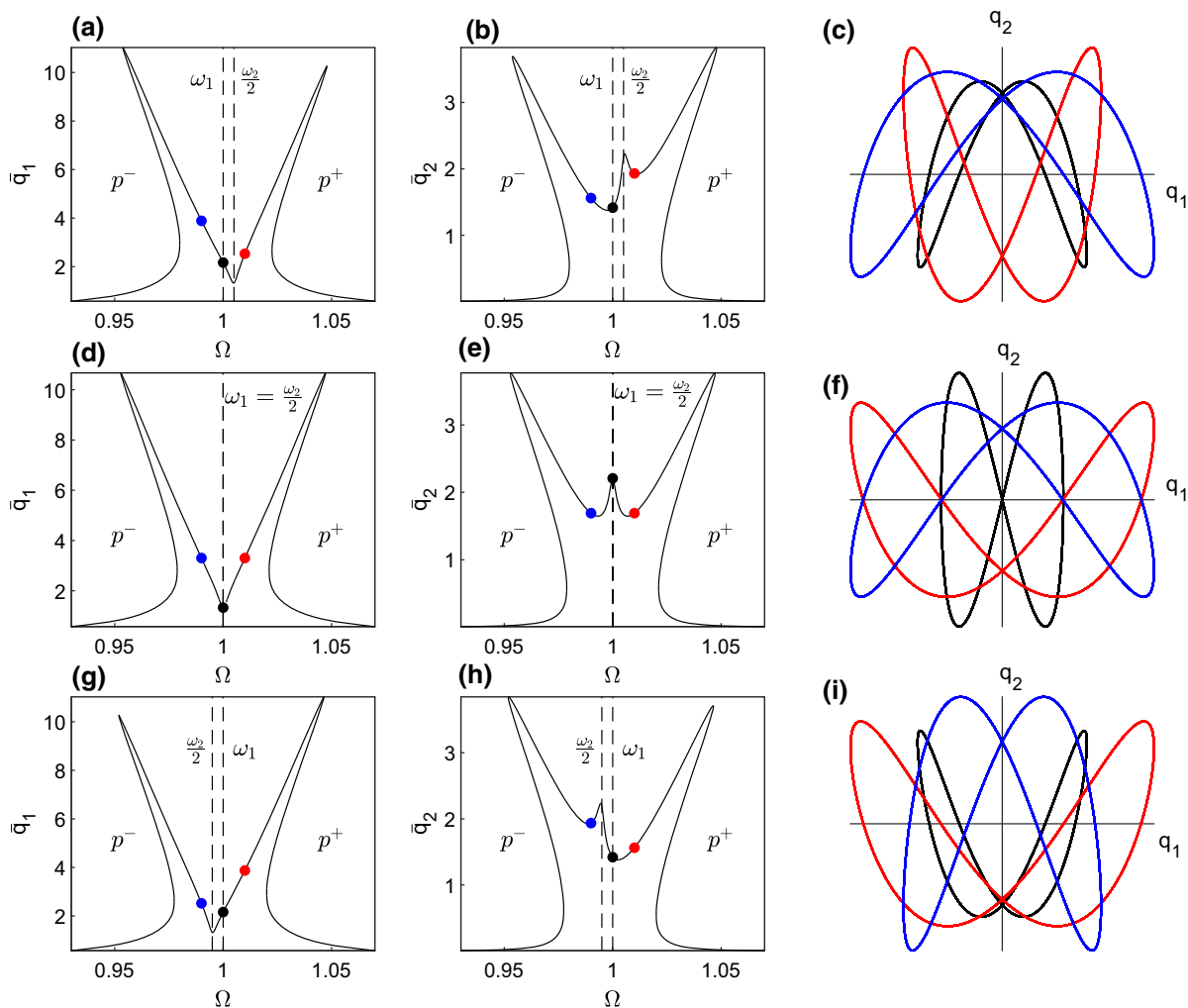
Fig. 4 Typical frequency-response functions and orbit in configuration space (q_1, q_2), for different cases of detuning. First line, positive detuning, $\omega_2/2 > \omega_1$. Second line, no detuning, $\omega_2/2 = \omega_1$. Third line, negative detuning $\omega_2/2 < \omega_1$. Stability is not reported. Selected values of the parameters: $\omega_1 = 1$, $\alpha_{12} = 5 \cdot 10^{-2}$, $\alpha_{11} = 2.5 \cdot 10^{-2}$, $\mu_1 = \mu_2 = 2.5 \cdot 10^{-3}$, $F = 8 \cdot 10^{-2}$

dephasing corresponding to the addition of forcing and damping (exact parabola is retrieved for the backbone only). The same reasoning applies for the red point corresponding to p^+-mode. The black point is selected exactly at $\Omega = \omega_1$ and is a p^--mode also.

The second line of Fig. 4 considers the tuned case $\omega_2/2 = \omega_1$. In Fig. 4 f), while p^+ and p^- mode are still perfectly well retrieved, the black point at $\Omega = \omega_1$ shows a combination of the two solutions resulting in a symmetrical shape in the (q_1, q_2) plane. Finally, the third line shows the case of a negative detuning, and behaves symmetrically as compared to the case of positive detuning. Increasing the detuning from

negative to positive values, we see how the solution emanating from the forced low-frequency ω_1 switches from the p^- to the p^+ mode, with the intermediate step being the symmetric shape shown in Fig. 4 f). This result is in line with those presented in [27] and complement their analysis by underlining the parabolic nature of the two families of periodic orbits, with different curvature.

3.2 Isolas

Interestingly, the first-order solution obtained by MS analysis contains isolated branches of solutions, as

already remarked in [27]. In addition to their analysis, it is here underlined that the manifestation of these isolas is the consequence of the non-vanishing starting point on the $\bar{q}_2$ axis when the internal detuning is different from zero. This particular feature is
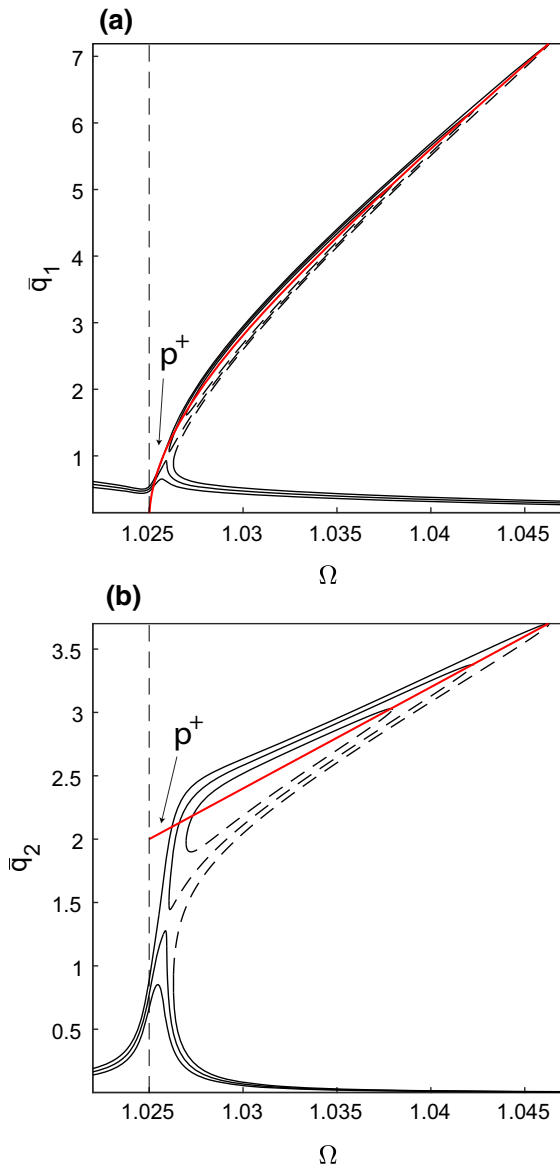

Fig. 5 FRF and backbone curves close to the isolated solution branches, obtained for $\sigma_1 = 0.05$, $\alpha_{12} = 5 \cdot 10^{-2}$ and $\alpha_{11} = 2.5 \cdot 10^{-2}$. The black continuous lines are the FRF (forced and damped solutions). The red lines are the backbones corresponding to the p^+ mode. The black dashed line marks $\Omega = \omega_2/2$. Damping values as $\mu_1 = \mu_2 = 1 \cdot 10^{-3}$. Selected values of the forcing amplitude are $F = 2.5 \cdot 10^{-2}, 2.75 \cdot 10^{-2}, 3 \cdot 10^{-2}$

illustrated in Fig. 5 for the case of a positive detuning, $\omega_2/2 > \omega_1$. As shown in the previous section, the limit value of the p^+-mode corresponds to a non-vanishing value of $\bar{q}_2$. Since the forced-damped solutions emanate from the backbone curves [5], this eventually creates the condition for the appearance of isolas.

3.3 Stability analysis and Neimark-Sacker boundary

The stability analysis of the solutions is based on the eigenvalues λ of the Jacobian matrix of Eq. (26), analysed in Appendix 3. The characteristic polynomial can be written as:

$$\lambda^4 + c_1\lambda^3 + c_2\lambda^2 + c_3\lambda + c_4 = 0, \tag{29}$$

with all the coefficients detailed in Appendix 4. Since all expressions are available in closed form, one can explicitly compute the stability of the solutions and follow bifurcation points.

We focus on the definition of the Neimark-Sacker (NS) boundary curve. The NS bifurcation requires that a pair of eigenvalues are complex conjugate with zero real part. Using the compact definition of the characteristic polynomial of Eq. (29), this implies that the four eigenvalues are $\mathbb{i}A, -\mathbb{i}A, B, C$ where $A \in \mathbb{R}$ and $B, C \in \mathbb{C}$. Then Eq. (29) can be rewritten as [26]:

$$\begin{aligned} &\lambda^4 + c_1\lambda^3 + c_2\lambda^2 + c_3\lambda + c_4 \\ &= (\lambda - \mathbb{i}A)(\lambda + \mathbb{i}A)(\lambda - B)(\lambda - C). \end{aligned} \tag{30}$$

Equating the same power terms one obtains a system of four equations:

$$c_1 = -(C + B), \tag{31a}$$

$$c_2 = A^2 - BC, \tag{31b}$$

$$c_3 = -A^2(C + B), \tag{31c}$$

$$c_4 = A^2 BC. \tag{31d}$$

Isolating A^2 as the ratio between Eq. (31a) and Eq. (31c), expressing the product BC using Eq. (31d) and inserting both terms in Eq. (31d), the condition for a NS bifurcation can be expressed in terms of the c_i's only, reading:
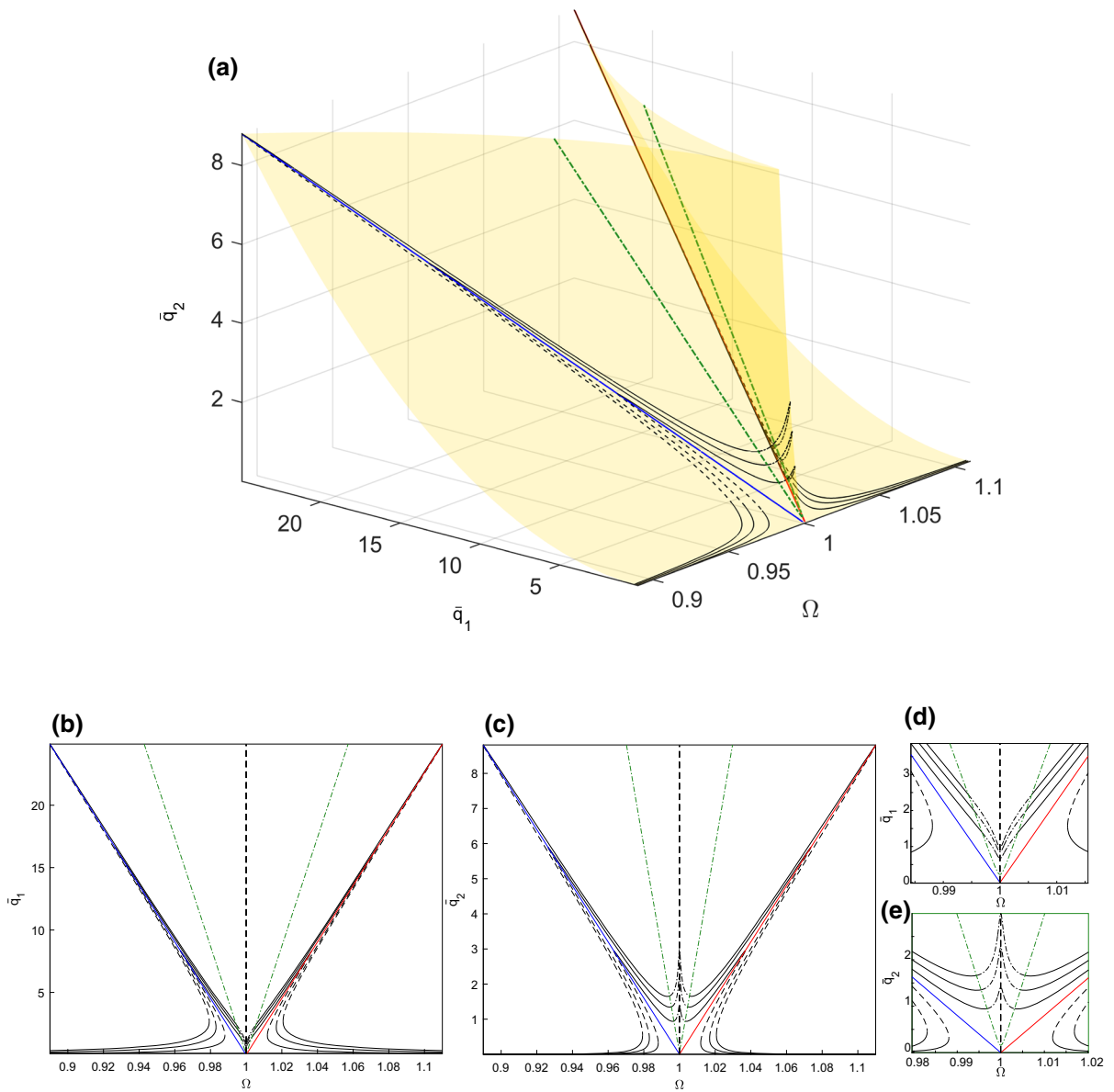
Fig. 6 FRF, backbone curves and NS boundary when $\omega_1 = 1$, $\omega_2 = 2\omega_1$, $\mu_1 = \mu_2 = 1 \cdot 10^{-3}$, $\alpha_{12} = 5 \cdot 10^{-2}$ and $\alpha_{11} = 2.5 \cdot 10^{-2}$. The black continuous lines are the FRF (forced and damped solutions). The red and the blue lines are the backbones corresponding to the p^+ and p^- mode respectively. The black dashed line marks the $\Omega = \omega_2/2$ frequency. The green dash-dotted line is the NS boundary. In 3D figure in the space $\Omega - a_1 - a_2$ the orange surface is the manifold on which all the possible forced and damped solution lies and is given by Eq. (27b). Selected values of the forcing amplitude are $F = 2.5 \cdot 10^{-2}, 5 \cdot 10^{-2}, 7.5 \cdot 10^{-2}$
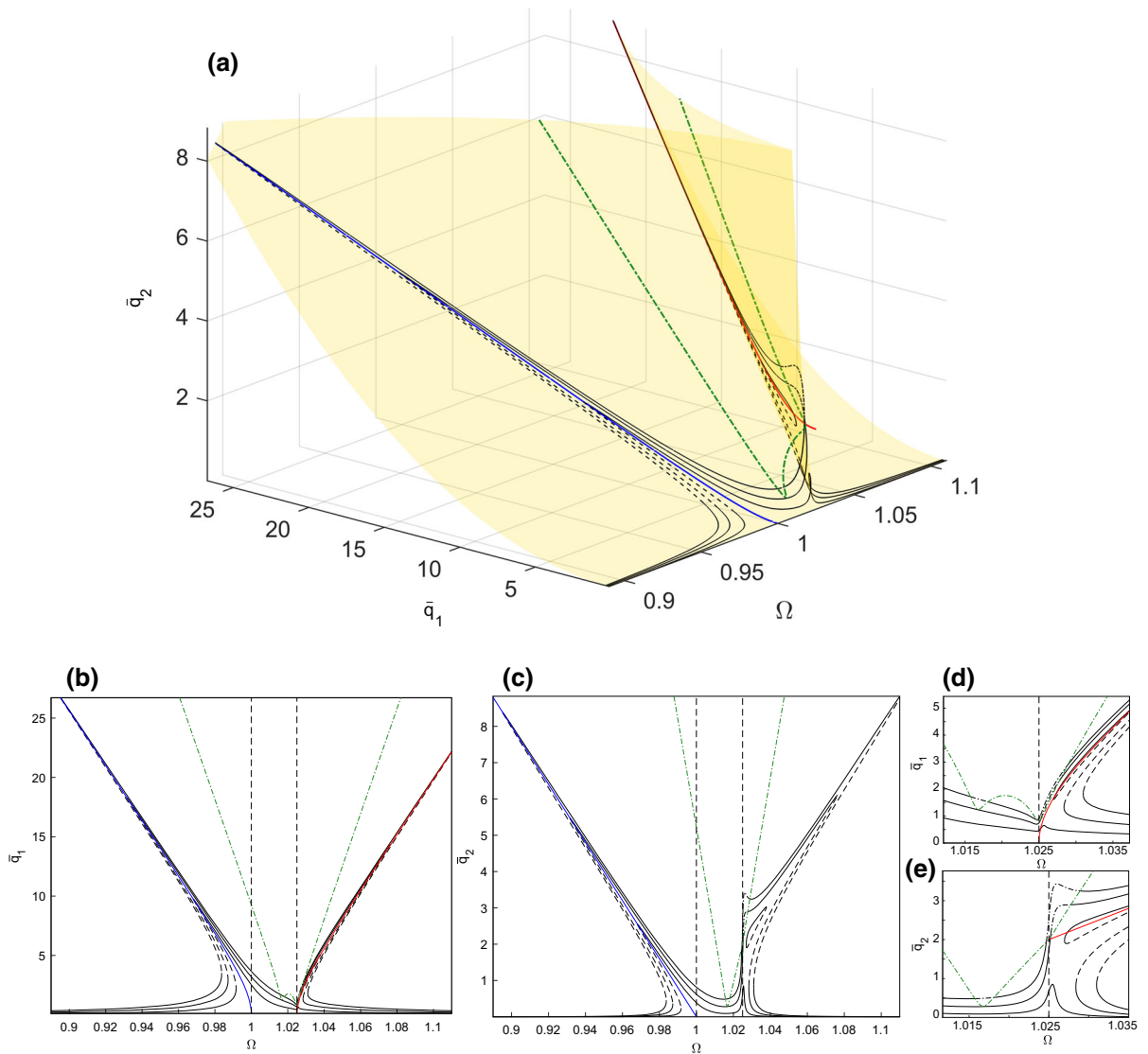
Fig. 7 FRF, backbone curves and NS boundary when $\sigma_1 = 5 \cdot 10^{-2}$, $\mu_1 = \mu_2 = 1 \cdot 10^{-3}$, $\alpha_{12} = 5 \cdot 10^{-2}$ and $\alpha_{11} = 2.5 \cdot 10^{-2}$. The black continuous lines are the FRF (forced and damped solutions). The red and the blue lines are the backbones corresponding to the p^+ and p^- mode respectively. The black dashed line marks the $\Omega = \omega_2/2$ frequency.

The green line is the NS boundary. In 3D figure in the space $\Omega - \bar{q}_1 - \bar{q}_2$ the orange surface is the manifold on which all the possible forced and damped solution lies and is given by Eq. (27b). Selected values of the forcing amplitude are $F = 2.5 \cdot 10^{-2}, 5 \cdot 10^{-2}, 7.5 \cdot 10^{-2}$

$$c_1 c_2 c_3 = c_3^2 - c_4 c_1^2, \tag{32a}$$

$$\frac{c_3}{c_1} = A^2. \tag{32b}$$

Inserting the detailed expressions of each coefficient in Eq. (32), the definition of the NS boundary curve is obtained as a polynomial in $\bar{q}_2$, and reads:

$$b_1 \bar{q}_2^4 + b_2 \bar{q}_2^3 + b_3 \bar{q}_2^2 + b_4 \bar{q}_2 + b_5 = 0. \tag{33}$$

where the expressions of b_i are reported in Appendix 4. For fixed values of the system parameters $\mu_1, \mu_2, \alpha_{12}, \omega_2, \omega_1$ and spanning the values of Ω one gets the boundary curve for the NS bifurcation as a function $\bar{q}_2(\Omega)$.
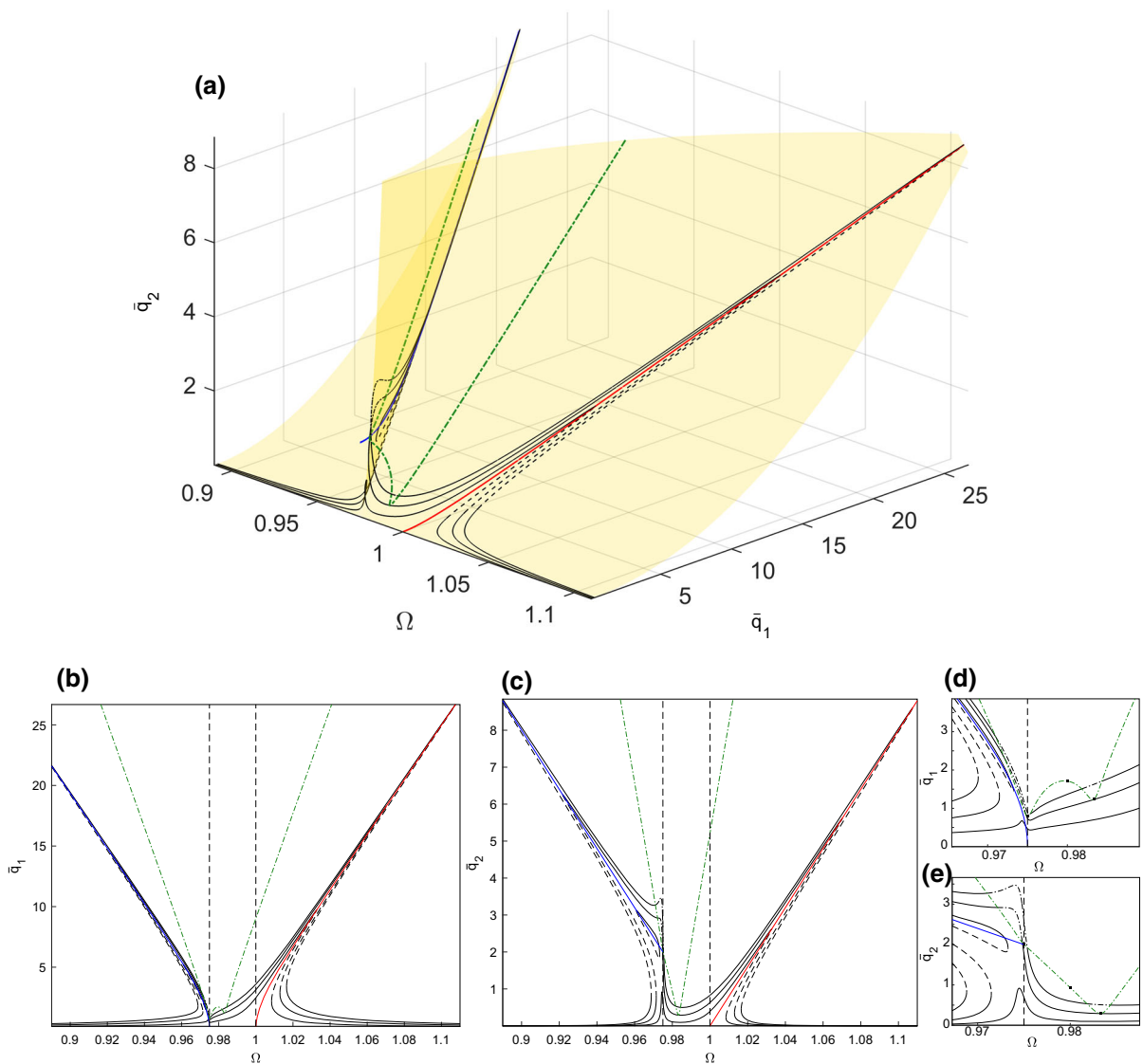
Fig. 8 FRF, backbone curves and NS boundary when $\sigma_1 = -5 \cdot 10^{-2}$, $\mu_1 = \mu_2 = 1 \cdot 10^{-3}$, $\alpha_{12} = 5 \cdot 10^{-2}$ and $\alpha_{11} = 2.5 \cdot 10^{-2}$. The black continuous lines are the FRF (forced and damped solutions). The red and the blue lines are the backbones corresponding to the p^+ and p^- mode respectively. The black dashed line marks the $\Omega = \omega_2/2$ frequency.

The green line is the NS boundary. In 3D figure in the space $\Omega - \bar{q}_1 - \bar{q}_2$ the orange surface is the manifold on which all the possible forced and damped solution lies and is given by Eq. (27b). Selected values of the forcing amplitude are $F = 2.5 \cdot 10^{-4}, 5 \cdot 10^{-4}, 1 \cdot 10^{-3}$

3.4 FRFs, backbone curves and NS boundary

We now discuss the complete solutions including the FRF, their connection with the backbone curves and the location of the NS boundaries.

We select a fixed set of parameters $\omega_1 = 1$, $\mu_1 = \mu_2 = 1 \cdot 10^{-3}$, $\alpha_{12} = 5 \cdot 10^{-2}$ and $\alpha_{11} = 2.5 \cdot 10^{-2}$. First, the case of a vanishing internal detuning, thus

$\omega_2 = 2\omega_1$, is shown in Fig. 6 collecting the FRF, Eq. (27), the NS boundary, Eq. (33); and the backbones given by Eqs. (16) and (12). Fig. 6 a) is a view in the 3D space (Ω, a_1, a_2). The solution manifold given by Eq. (27b) is represented as an orange surface and all solution branches as well as the NS boundary curve lie on this manifold. In this case the figure is fully symmetric with respect to $\Omega = \omega_1 = \omega_2/2$. Figure 6
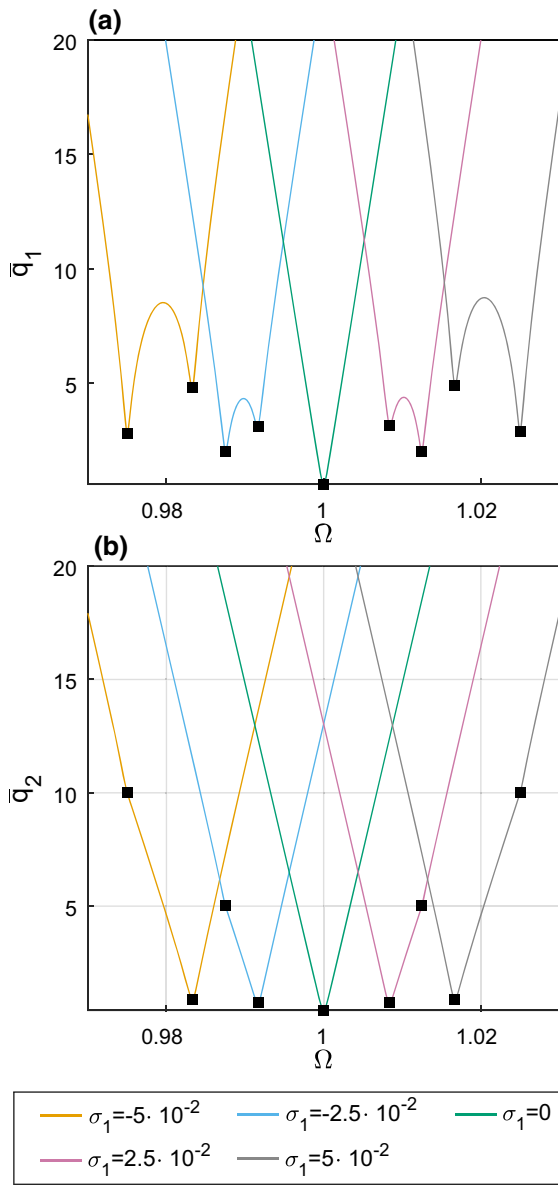
Fig. 9 Behaviour of the NS boundary curve when the detuning $\sigma_1 = \omega_2 - 2\omega_1$ is changed. The system parameter here considered are $\alpha_{12} = 1 \cdot 10^{-2}$, $\alpha_{11} = 5 \cdot 10^{-3}$, $\mu_1 = \mu_2 = 5 \cdot 10^{-3}$. The square markers correspond to the minima predicted by the analytical expression given in Appendix 5, namely $\Omega = \omega_2/2$ and $\Omega = (\omega_1 + \omega_2)/3$
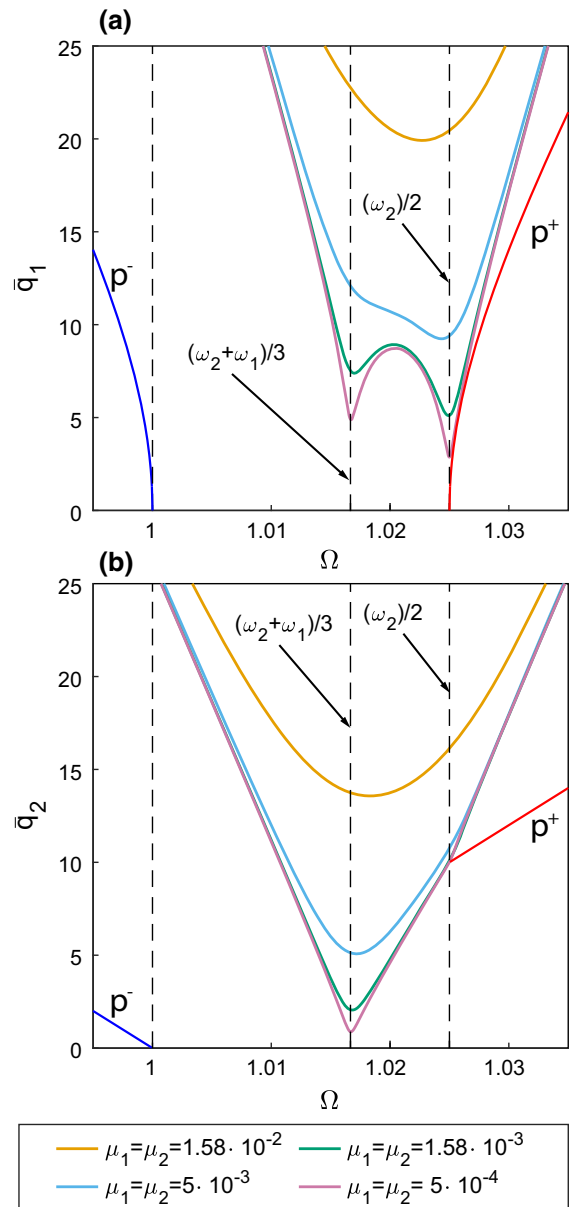
Fig. 10 Behaviour of the NS boundary curve, for $\omega_1 = 1$, $\omega_2 = 2.05$, $\alpha_{12} = 1 \cdot 10^{-2}$, $\alpha_{11} = 5 \cdot 10^{-3}$ and different values of $\mu_1 = \mu_2$ as detailed in the legend. The blue and red continuous lines are the backbone of the p^- and p^+ mode while the black dashed lines correspond to $\Omega = \omega_2/2$ and $\Omega = (\omega_1 + \omega_2)/3$

b), c) show the projection of the 3D plot respectively on planes $(\Omega, \bar{q}_1)$ and $(\Omega, \bar{q}_2)$. The FRF develops according to the backbone curves of the p^+ and p^- modes. When Ω approaches ω_1 the FRF have a local peak for $\bar{q}_2$, and correspondingly $\bar{q}_1$ approaches a nearly zero value. In this case, the NS boundary is

symmetric and displays a unique minimum centred at $\Omega = \omega_1$, as shown in the enlarged view Fig. 6 d) and e).

Fig. 7 shows the case of a positive detuning, with $\omega_2 = 2\omega_1 + 5 \cdot 10^{-2}$, all the other parameters being
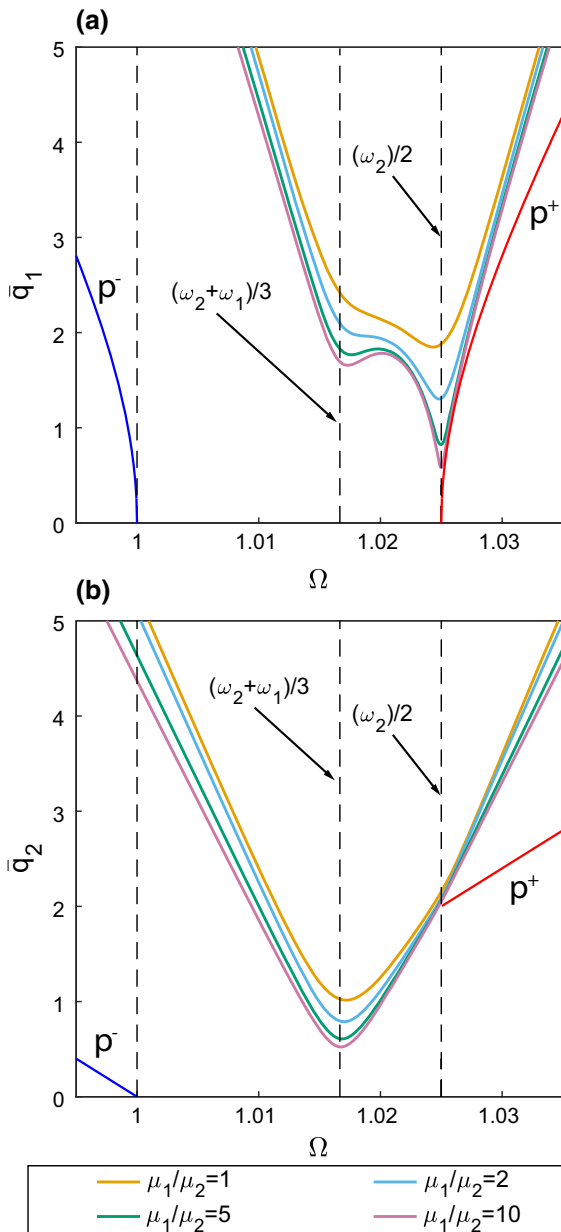
(a)

(b)

Fig. 11 Behaviour of the NS boundary curve, for $\omega_1 = 1$, $\omega_2 = 2.05$, $\alpha_{12} = 5 \cdot 10^{-2}$, $\alpha_{11} = 2.5 \cdot 10^{-2}$ and different ratio μ_1/μ_2 keeping $\mu_1 = 5 \cdot 10^{-3}$ fixed. The blue and red continuous lines are the backbone of the p^- and p^+ mode while the black dashed lines mark $\Omega = \omega_2/2$ and $\Omega = (\omega_1 + \omega_2)/3$. The other lines corresponds to different damping levels as detailed in the legend

unchanged. In this case the symmetry is broken, as can be appreciated by inspecting the shape of the solution manifold in the 3D space, showing a minimum with respect to $\bar{q}_1$ at $\Omega = \omega_2/2$. The solution branches
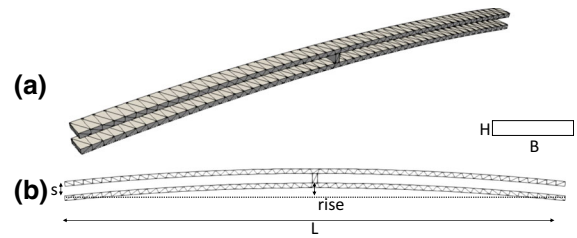

Fig. 12 a 3D view of the FEM model used for the arch, **b** scheme of the geometry of the shallow arch considered. B=20 μm, H=5 μm, L=530 μm, rise=13.4 μm, s=10 μm

arising in the vicinity of $\Omega = \omega_1$ belong to the p^- family, in line with previous remarks. The shape of NS boundary curve (see Fig. 7d) and e)), also shows important modifications, having two minima and one local maximum, particularly visible in the $(\Omega, \bar{q}_1)$ projection. Interestingly, the projection on the $(\Omega, \bar{q}_2)$ plane shown in Fig. 7c) underlines the closeness of the NS boundary to the non-zero point where the backbone of the p^+-mode emerges.

Finally, the case of a negative detuning with $\omega_2 = 2\omega_1 - 5 \cdot 10^{-2}$ is addressed in Fig. 8. The solutions around ω_1 now belong to p^+-mode. The NS boundary shows again the two minima and the local maximum, and its closeness to the emerging point of the p^--mode is symmetrically observed.

These results underline that a further investigation of the minima and maxima of the NS boundary curve, together with its relationship with the backbones, would provide a better understanding of the dynamics. This is the aim of the following sections.

Table 1 First six eigenfrequencies of the arch. The third column reports the ratio with respect to the first eigenmode. The fourth column refers to their graphical representation in Fig. 13

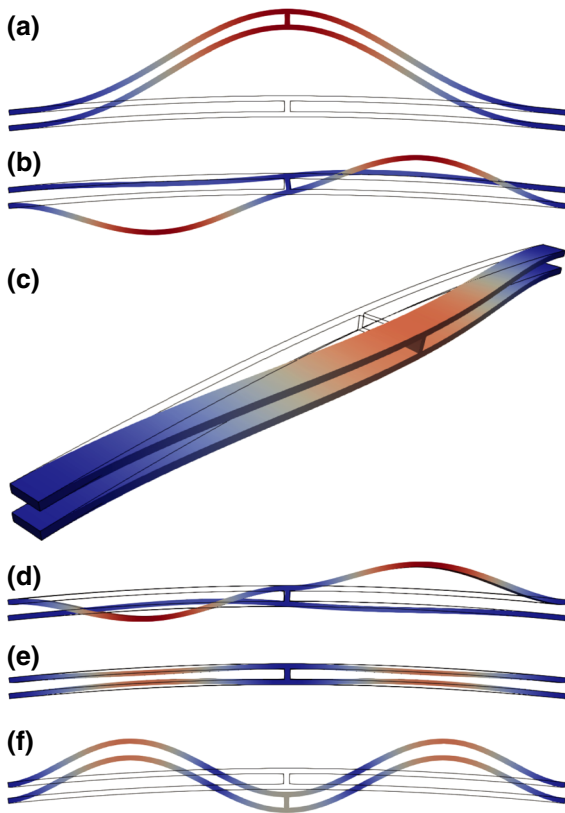| Mode n	Frequency [MHz]	Ratio	Fig.
1	0.43416	1	13 a)
2	0.52597	1.211	13 b)
3	0.60391	1.391	13 c)
4	0.66759	1.537	13 d)
5	0.75695	1.743	13 e)
6	0.86367	1.989	13 f)

Fig. 13 First six eigenmodes of the arch. The contour of the displacement magnitude is shown in colour

3.5 NS boundary behaviour and extrema

In this section the parametric dependence of the NS boundary curve with respect to detuning and damping is investigated with specific attention to special points corresponding to extrema of the boundary. Fig. 9 first displays the shape of the NS boundary curve when the detuning is varied from negative to positive values, in both planes $(\Omega, \bar{q}_1)$ and $(\Omega, \bar{q}_2)$. The plots have been obtained for $\omega_1 = 1$, $\mu_1 = \mu_2 = 5 \cdot 10^{-4}$, $\alpha_{12} = 1 \cdot 10^{-2}$ and $\alpha_{11} = 5 \cdot 10^{-3}$ and different values of ω_2. As already underlined, the boundary curve has a single minimum in the case of no detuning, obtained from Eq. (33) assuming $\omega_2 = 2\omega_1 = 2\Omega$:

$$\bar{q}_2 = \frac{4(\mu_1 + \mu_2)\omega_1}{\alpha_{12}}, \tag{34a}$$

$$\bar{q}_1 = 4\sqrt{\frac{(\mu_1 + \mu_2)\omega_1\omega_2}{\alpha_{12}\alpha_{11}\Gamma}}. \tag{34b}$$

For non-vanishing detuning two minima occur in the plane $(\Omega, \bar{q}_1)$, and they correspond to points where there is a change of curvature in $(\Omega, \bar{q}_2)$ projection. This result is of prime importance since the locations of the minima convey meaningful information about the minimum forcing and amplitude levels that are needed to reach a quasiperiodic solution.

In Fig. 9, two points for each curve are marked with a black square, corresponding to $\Omega = \omega_2/2$ and $\Omega = (\omega_1 + \omega_2)/3$. These are minima of the NS boundary curve predicted by asymptotic analysis as detailed in Appendix 5.

These specific points are obtained in the limit of small damping and are thus only approximate values. This is further illustrated in Fig. 10, obtained for $\omega_1 = 1$, $\omega_2 = 2.05$, $\alpha_{12} = 1 \cdot 10^{-2}$, $\alpha_{11} = 5 \cdot 10^{-3}$ and different values of damping assuming $\mu_1 = \mu_2$. The detuned frequency condition is considered because the loci of the minima change only in this case. The figure shows that the NS boundary tends to have sharper minima and values closer to the proposed approximation as damping tends to zero. On the other hand, the behaviour of the NS boundary curve at large values of amplitudes is asymptotically identical and not very sensitive to variations of the damping.

A different case is analysed in Fig. 11, obtained for $\omega_1 = 1$, $\omega_2 = 2.05$, $\alpha_{12} = 5 \cdot 10^{-2}$, $\alpha_{11} = 2.5 \cdot 10^{-2}$ and different values of the ratio μ_1/μ_2, while keeping $\mu_1 = 5 \cdot 10^{-3}$ fixed. The figure shows that increasing the damping μ_2 makes the NS boundary smoother. It moreover underlines that in this specific case the asymptotic behaviour of the curve at large amplitudes

Table 2 Coefficients describing the internal nonlinear elastic force in the ROM

eigenmode	(1)	(2)
k_1	1	-3.1705×10^{-8}
k_2	-4.2188×10^{-9}	3.9572
a_{11}	0.0156	0.0095
a_{12}	0.0191	0.0410
a_{22}	0.0205	-0.0568
b_{111}	6.7646×10^{-5}	8.7921×10^{-5}
b_{112}	2.6376×10^{-4}	5.6267×10^{-4}
b_{122}	5.6241×10^{-4}	0.0014
b_{222}	4.7679×10^{-4}	0.0021

is also affected. It is worth stressing that, except for the largest value of μ_2, all the curves in the $(\Omega, \bar{q}_2)$ plane stay close to the specific point where the p^+ backbone emerges, underlining again the particular role of this point in the dynamics.

4 Test example: a clamped shallow double-arch MEMS structure

In this section we validate our previous findings by predicting the appearance of FCs in a MEMS clamped shallow arch. To highlight possible limits of the MS solution, we progressively add features in the model and comparisons and discussions are proposed for each step. First we check the MS solution reliability assuming that the structure behaviour is governed by Eq. (1) featuring only two quadratic nonlinear terms. The MS results, given by Eq. (27) are compared with the numerical solution of Eq. (1) when the detuning parameter vanishes, i.e. $\omega_2 = 2\omega_1$, and in the general case $\omega_2 \neq 2\omega_1$, the latter condition being more realistic from a practical point of view since process imperfections typically prevent a perfect match between the two eigenfrequencies. Finally a comparison between a reduced-order model including all nonlinearities, the corresponding MS solution and a full Finite Element Simulation is proposed using a custom code [43].

4.1 Reduced order model

The arch geometry and dimensions are reported in Fig. 12.

The device is made of polycrystalline silicon with density $\rho = 2330$ kg/m³. A linear elastic constitutive model (Saint-Venant Kirchhoff) is considered, with Young modulus $E = 167000$ MPa and Poisson coefficient $v = 0.22$ [49]. The double-arch has a large radius of curvature and it can be considered as shallow. The structure is inspired by the design proposed in [12], and it exploits two clamped arches connected at their center points in order to shift the anti-symmetric modes to higher frequencies. The first six eigenfrequencies of the structure, obtained from a Finite Element (FE) analysis using the mesh in Fig. 12 b, are reported in Tab. 1, and the corresponding mode shapes are shown in Fig. 13. In particular, one can

observe that it is possible to achieve a 1:2 resonance between the first and the sixth eigenmodes, Fig. 13 a and f.

A reduced-order model (ROM) is obtained from the full FE model using a static condensation approach [13, 25]. The ROM retains as master modes only the two eigenmodes involved in the 1:2 resonance. The approach uses static loadings proportional to the inertia of the master modes to create a stress manifold
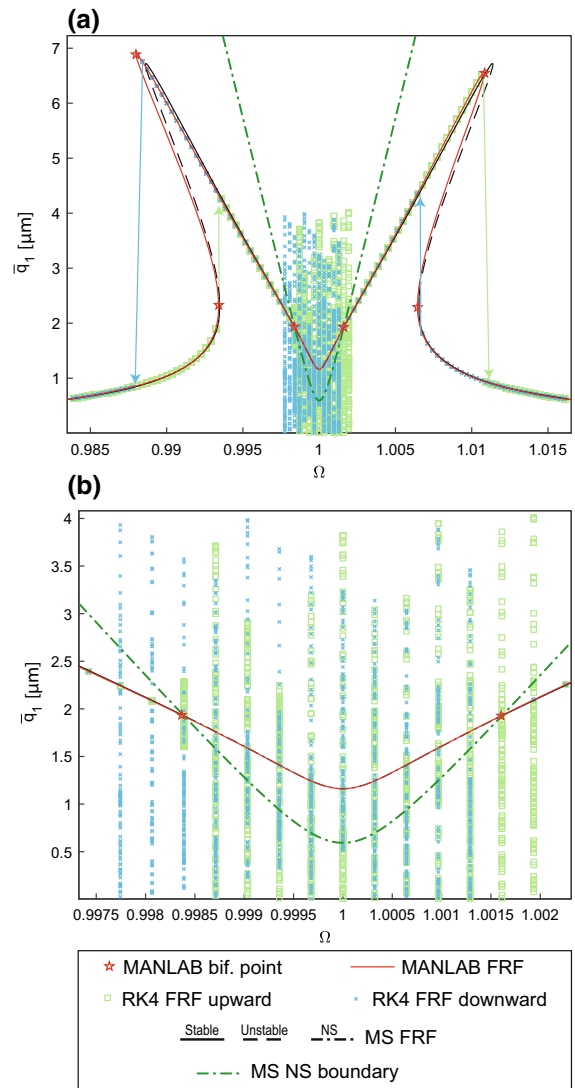

Fig. 14 Tuned condition $\omega_2 = 2\omega_1$. Comparison between the analytical solution from Eq. (27) (black line), continuation of periodic orbits of Eq. (1) (red lines) and the time-marching integration of Eq. (1) (circle markers). The analytical NS boundary is the green dash-dotted line. The red star markers define the bifurcation points identified by MANLAB

Table 3 Estimate of the incommensurate frequency ω_{NS} for the upward and downward external frequency sweeps Ω considered, in the perfectly tuned case $\omega_2 = 2\omega_1$. The RK4 estimates are extracted from the FT of the system (resolution $\approx 5 \cdot 10^{-4}$). The value not specified in the RK4 values correspond to a chaotic regime were the FC spacing is not defined. Analytical values of ω_{NS} provided by the MS method at the onset of the QP regime as reported in the last lines

	Ω [−]	ω_{NS} [−]10^{-3}			ω_{NS} [−]10^{-3}		
RK4	0.99838	5.39	↓	upward	–	↑	downward
	0.99871	3.99			4.19		
	0.99903	4.00			4.00		
	0.99936	3.60			3.60		
	0.99968	2.00			2.00		
	1.00000	5.40			5.40		
	1.00032	2.00			2.00		
	1.00064	3.60			3.60		
	1.00097	4.00			4.00		
	1.00129	3.20			3.20		
	1.00161	3.00			5.40		
MS	0.99838	5.49			5.49		
	1.00161						

which is then fitted with a third order polynomial to obtain an explicit expression of the nonlinear restoring forces. The reduced-order dynamics, expressed with nondimensional time $\tau = \omega_1 t$ and mass-normalized values, reads:

$$
\begin{aligned}
& q_1'' + \mu_1 q_1' + k_1^{(1)} q_1 + k_2^{(1)} q_2 + a_{11}^{(1)} q_1^2 \\
& \quad + a_{12}^{(1)} q_1 q_2 + a_{22}^{(1)} q_2^2 + b_{111}^{(1)} q_1^3 + b_{112}^{(1)} q_1^2 q_2 \\
& \quad + b_{122}^{(1)} q_1 q_2^2 + b_{222}^{(1)} q_2^3 = F \cos \Omega \tau, \\
& q_2'' + \mu_2 q_2' + k_1^{(2)} q_1 + k_2^{(2)} q_2 + a_{11}^{(2)} q_1^2 \\
& \quad + a_{12}^{(2)} q_1 q_2 + a_{22}^{(2)} q_2^2 + b_{111}^{(2)} q_1^3 + b_{112}^{(2)} q_1^2 q_2 \\
& \quad + b_{122}^{(2)} q_1 q_2^2 + b_{222}^{(2)} q_2^3 = 0,
\end{aligned}
\tag{35a}
$$

where q_1 and q_2 are the generalized modal coordinates expressed in [μm] and $k_i^{(k)}$, $a_{ij}^{(k)}$ and $b_{ijs}^{(k)}$ are the linear, quadratic and cubic coefficients, respectively, for eigenmode k. The load multiplier considered in our benchmark is $F = 0.0201$ μNμs²/ng. The first and second order derivatives with respect to the nondimensional time are denoted with $'$ and $''$ respectively. Even if Ω is now a nondimensional frequency, the same symbol of the previous sections has been used since we fixed $\omega_1 = 1$ in all the examples presented therein.

The damping factor is $\mu_i = \frac{\omega_i}{Q_i \omega_1}$ with Q_1 and Q_2 factors set to 500 and 1000 respectively, which is consistent with a mass proportional damping. The coefficients of the polynomial are reported in Tab. 2.

Arch displacements can be reconstructed with good accuracy from the linear modes and in particular the midspan deflection is

$$
u(t) = 0.11 q_1(t) + 0.0707 q_2(t) \ [\text{μm}]. \tag{36}
$$

We notice that the selected damping values are slightly lower than the ones assumed in the previous examples concerning the MS solutions. This condition is typical of MEMS structures that are often packaged in near vacuum. The impact of these choices will be discussed in the following sections.

4.2 Multiple scales model

In order to apply the MS formulas, the nonlinear terms of Eq. (35) that are not included in Eq. (1) are neglected. First we consider the perfectly tuned case by enforcing $\omega_2 = 2\omega_1$. We compare the FRF given by Eq. (27) and the solution computed via direct numerical continuation of periodic orbits applied to Eq. (1) using the continuation package MANLAB [20]. The numerical continuation solution is also
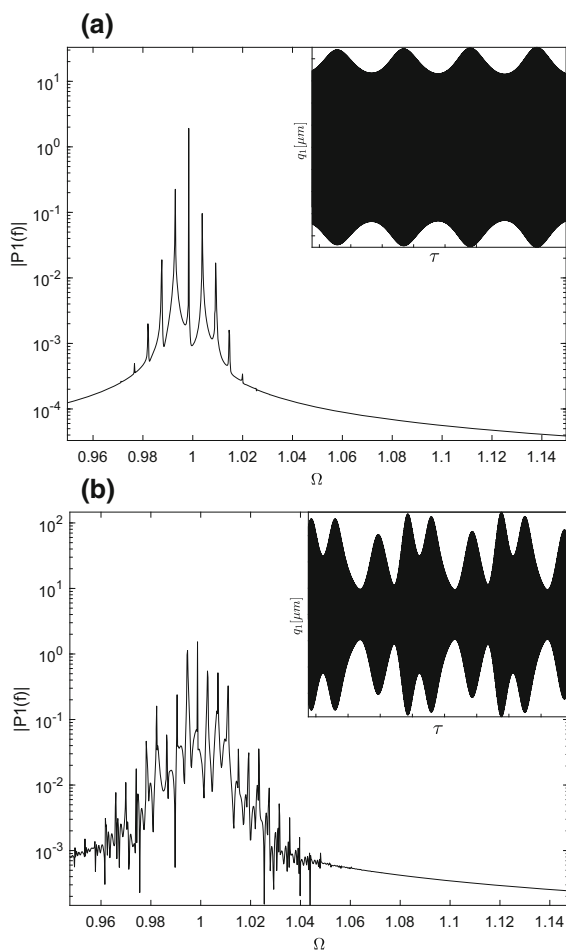
Fig. 15 FT and time histories from the RK4 solution on $\Omega = 0.99838$ a) and $\Omega = 0.98711$ b)

assessed by comparison with a direct time-marching algorithm on system Eq. (1) in order to investigate the QP regime behaviour. For this case, a Runge-Kutta order 4 (RK4) integration scheme is used and QP solutions are plotted as Poincaré sections obtained by stroboscopy at the forcing frequency. Upward and downward sweeps of the forcing frequency are performed and for each frequency $5000 (= 10Q_1)$ cycles are simulated to reach the steady state regime and collect time history data. The time step adopted is $1/500$ of the forcing period $2\pi/\Omega$.

Results are plotted in Fig. 14a). The MS and continuation (MANLAB) FRF are superimposed everywhere except close to the peaks. The numerical solution of Eq. (1) predicts a larger amplitude at the lower frequency peak and a smaller amplitude at the high frequency one. Indeed at the peaks the

assumption of the MS solution that nonlinear terms are small starts being violated. On the contrary, the NS boundary intersections with the FRF predicted by the MS have a nearly perfect agreement with the bifurcation analysis performed by MANLAB (see the enlarged view in Fig. 14 b). This is reasonable since the NS boundary crosses the FRF at low amplitudes, where the MS approximation is fully respected.

Inspection of the time-marching solution reveals additional information. The match with the FRF obtained thanks to numerical continuation is almost exact in the periodic regions, the only difference being that the RK4 results present jumps in the solution (highlighted with arrows in the plot) since unstable solutions cannot be simulated. The time-marching solution allows appreciating amplitude modulation in the QP region. For a fixed frequency value a cloud of points is observed, as expected in a QP regime. The incommensurate frequency can be estimated from the Fourier Transform (FT) of the response and results are reported in Table 3 for both the upward and downward span.

The MS solution developed in this work cannot predict the behaviour of ω_{NS} inside the QP region, but it can be used to estimate the values at its boundary, since here the purely imaginary eigenvalues define the oscillating frequency of a_i. The NS bifurcations occur at $\Omega = 0.99838$ and $\Omega = 1.00161$ respectively, corresponding to the eigenvalues $\lambda = \pm\mathbb{i}5.49 \cdot 10^{-3}$, that have the same value at both frequencies. The computed analytical value of λ can be compared with the numerical results of Tab. 3. It is worth stressing that the agreement is good at the left of the NS in the upward sweep and at the right of the NS in the downward sweep, *i.e.* at the onset of the instability. The agreement then changes proceeding in the NS region since the numerical solution follows the QP solution branch on which the additional frequency of the torus is varying, a feature not provided by the MS analysis. Examples of the FT and time histories encountered in the frequency span are illustrated in Fig. 15 a and b referring to $\Omega = 0.99838$ and $\Omega = 0.98711$ respectively.

In Fig. 15 a, the QP regime has just settled down and one can observe a clear modulation of the envelope in the time domain, and a well shaped spectrum with clean spacings between all the frequency peaks, following the rule $n\Omega \pm m\omega_{NS}$ with n and m integers. Fig. 15 b has been obtained for $\Omega =$
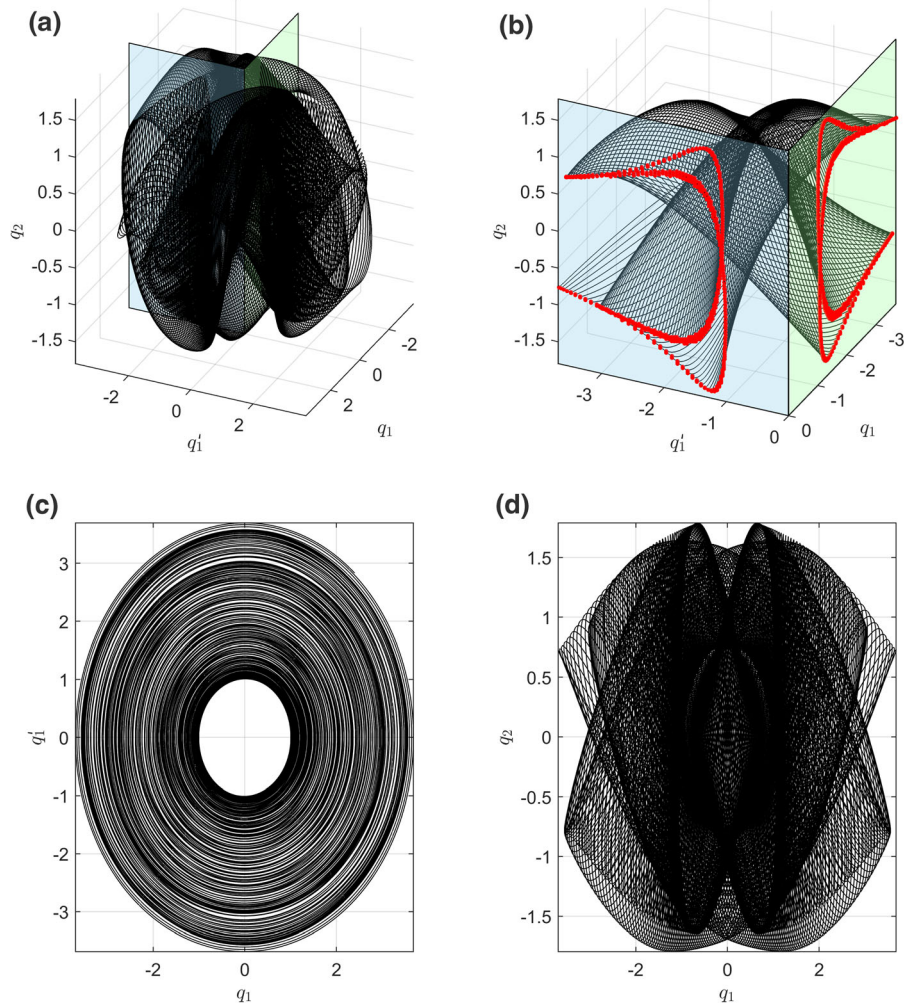
Fig. 16 Torus obtained by direct integration with RK4 algorithm of Eq. (1) in the tuned case $\omega_2 = 2\omega_1$. Only a short portion of the time history is plotted for sake of clarity

0.98711 in the upward frequency sweep, thus the QP regime is further along the branch of QP solution. One can appreciate how the QP is modified along the solution branch, with a more complex envelope modulation, and a more important number of frequency peaks in the spectrum. One can also observe the enlargement of the frequency peaks, indicating that the QP solution will probably lose its stability in favour of a chaotic behaviour further in the solution branch. One can also note that the direct time integration results underline the facts that the NS bifurcation is supercritical with emergence of a stable torus at both side of the branching points, symmetric, with probably a small portion of unstable torus close to the branching points.

Before moving to the detuned condition, phase space representation from time-marching solution are inspected.

The torus emerging from the NS bifurcation is represented in Fig. 16, obtained from direct RK4 integrations with $\Omega = 1$. A 3D representation in the space $(q_1, \dot{q}_1, q_2)$ and in the planes $(q_1, \dot{q}_1)$ and (q_1, q_2) are shown. For sake of clarity, only a short portion of the time history, corresponding to few quasi-periods, is considered. Fig. 16 a represents the phase space $(q_1, \dot{q}_1, q_2)$ while Fig. 16b) is a cross-section of the four dimensional torus considering the portion included in the green and the blue planes. The red dots mark the crossing region. Figure 16c) and d) are
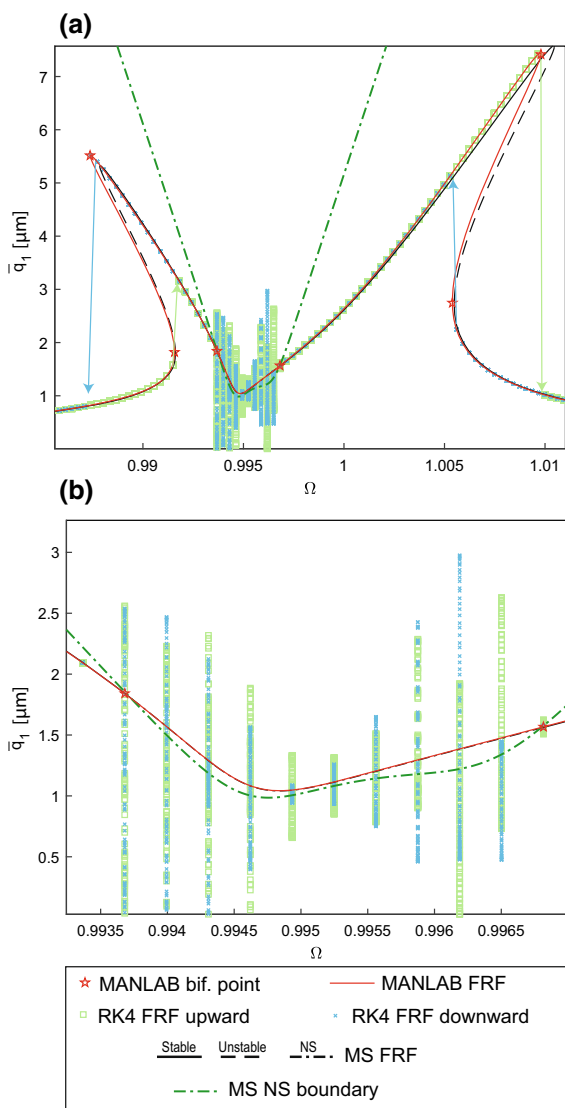
Fig. 17 Detuned condition $\omega_2 = 1.989\omega_1$. Comparison between the analytical solution from Eq. (27) (black line), continuation of periodic orbits of Eq. (1) (red lines) and the time-marching integration of Eq. (1) (circle markers). The analytical NS boundary is the green dash-dotted line. The red star markers define the bifurcation points identified by MANLAB

the 2D version of the phase space considering its two projections in the planes $q_1, \dot{q}_1$ and q_1, q_2.

The detuned case is now investigated with $\omega_2 = 1.989\omega_1$, and the same analysis is repeated. The FRF results are plotted in Fig. 17 and the ω_{NS} values are collected in Tab. 4. By comparing the MS and the numerical continuation (MANLAB) solutions, the FRFs and the NS bifurcation crossing points share

the same degree of accuracy of the previous case. Focusing on the incommensurate frequencies, the MS solution predicts $\omega_{NS} = 4.37 \cdot 10^{-3}$ at $\Omega = 0.99372$ and $\omega_{NS} = 6.19 \cdot 10^{-3}$ at $\Omega = 0.99679$. Fig. 17b) shows how the QP time-marching solution is completely embedded in the region estimated by MS. An outstanding match is found close to $\Omega = 0.99679$ while the values on $\Omega = 0.99372$ are lower than expected. The underlying reason is that at $\Omega = 0.99679$ a supercritical NS bifurcation appears, which is also confirmed by the identical values of ω_{NS} found close to this point when sweeping the forcing frequency in the increasing or decreasing direction. On the other hand, a subcritical NS bifurcation takes place at $\Omega = 0.99679$, consequently the added frequency predicted by the MS method corresponds to unstable quasi-periodic solutions that are not found with direct time integration. Instead, the numerical solution jumps to the branch of stable QP solutions and then travels up to the other supercritical bifurcation point.

4.3 Reduced order model and full order simulation

Finally we consider a comparison between the MS solution and the ROM retaining all nonlinear terms. Results obtained with the ROM are further validated with analyses performed on the full FE model using two different techniques. First, an Harmonic Balance approach (HB) is used, from which a reference FRF is computed. However, this technique in our implementation cannot detect QP solutions. As a consequence, a costly direct time integration of the full FE model is also performed with a Newmark-β scheme for specific values of Ω. The time-marching solution adopts a time step equal to 1/300 of the forced eigenmode period and 3000 cycles are simulated for each frequency. The full FEM model uses as external forcing a body force having the same shape of the first eigenmode, which is consistent with the ROM loading in Eq. (35). The comparison between the MS solution and the ROM is plotted in Fig. 18. As expected and mostly because of the presence of the cubic terms in the ROM, some quantitative differences appear between the two solutions. However no qualitative difference is reported since the simplified system studied in the MS development contains the most important resonant monomial terms that convey the important bifurcation

Table 4 Estimate of the incommensurate frequency ω_{NS} for the upward and downward frequency sweeps Ω considered, in the case $\omega_2 = 1.989\omega_1$. The RK4 estimates are extracted from the FT of the system (resolution $\approx 5 \cdot 10^{-4}$). Analytical values obtained from MS analysis at the bifurcation points reported in the last two lines

	Ω $-$	ω_{NS} $[-]10^{-3}$			ω_{NS} $[-]10^{-3}$		
RK4	0.99368	1.99	↓	upward	1.99	↑	downward
	0.99399	1.99			1.99		
	0.99431	2.39			2.39		
	0.99462	2.82			2.78		
	0.99493	3.78			3.78		
	0.99525	4.38			4.38		
	0.99556	4.98			4.98		
	0.99587	5.78			5.78		
	0.99619	5.98			5.98		
	0.99650	5.98			5.98		
	0.99681	6.18			6.18		
MS	0.99372	4.37					
	0.99679				6.19		
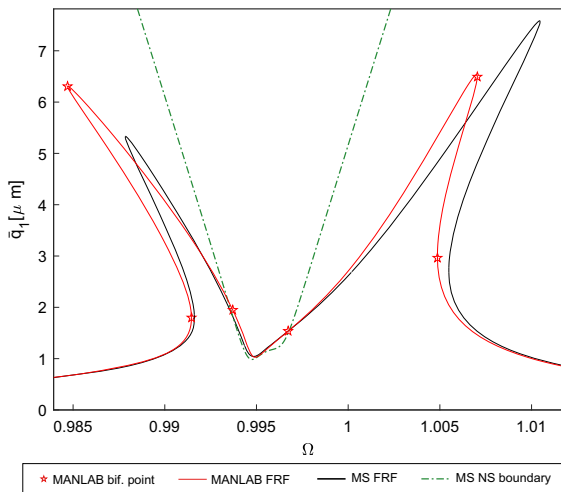
Fig. 18 Comparison between the analytical solution (black line) and the static condensation ROM (red line). The analytical NS boundary is the green dash-dotted line. The red star markers define the bifurcation points identified by MANLAB

information. Moreover in the low amplitude region and close to $\Omega = 1$ the MS solution is nearly exact. Also the prediction of the NS boundary intersections with the FRF shows a very good match with numerical results on the ROM. This is expected since the MS approach is reliable in a low amplitude region where the smallness assumptions still hold, and thus underlines that the analytical formula of the NS boundary curve can be used for rapid prediction of the occurrence of FC in such a case.

Finally we compare the ROM solution with a Full FEM simulation considering the maximum absolute midspan displacement max $|u|$. The results are plotted in Fig. 19 where the NS boundary curve from the MS solution is also included. We notice the excellent agreement between the FRF obtained using numerical continuation and HB for the full FEM model and for the ROM, respectively, validating the reduction technique adopted. As expected, the NS boundary from the MS predicts correctly the onset of the QP regime also in this case.

Fig. 20 shows three representative quasi-periodic solutions obtained from direct time integration on the full FE model. Note that these solutions are obtained from a decreasing sweep so that the solutions follow the QP branch of solution by order of decreasing frequencies. The first line in Fig. 20 corresponds to Ω=0.9965, which is the onset of the QP regime, just after the NS bifurcation point. The amplitude modulation displays a simple pattern in Fig. 20 a) and the frequency spectrum shows the appearance of the extra peaks indicating the birth of the FC. At this point one can compare the ω_{NS} value predicted by the MS at the boundary (see Table 4) and that from from direct numerical integration. The comb spacing in Fig. 20b reveals the value $\omega_{NS} = 5.93 \cdot 10^{-3}$, very close to the values reported in Table 4 and thus underlining again the good predictive capacity of the simple analytical model. The second line in Fig. 20 corresponds to Ω=0.9956, a point further along the branch of QP solutions. One can observe that the amplitude
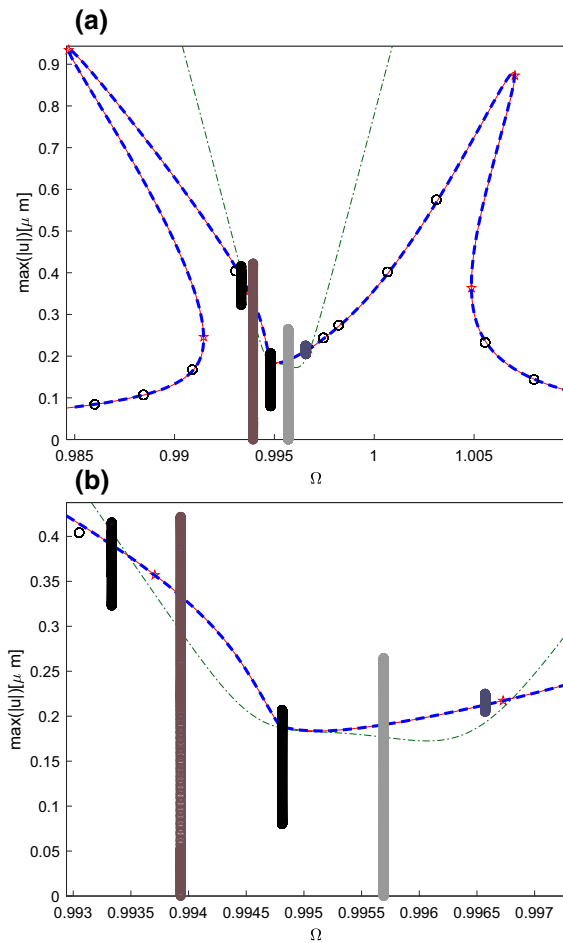
(a)

(b)

Fig. 19 Comparison between the static condensation ROM (red line), the HB FEM model (dashed blue line) and the time-marching FEM integration (circle markers). The analytical NS boundary is the green dash-dotted line. The red star markers define the bifurcation points identified by MANLAB. The circle markers highlighted with different colors correspond to the frequencies plotted in Fig. 20

modulation is more complex but still clearly periodic, resulting in a well defined frequency comb. In this case the new frequency ω_{NS} cannot be determined from the MS analysis. Finally, the third line shows the results obtained for $\Omega=0.9939$. In this case one can clearly observe that the envelope modulation has no clear periodicity at the reported time scales, underlining that the torus is on the way to lose its stability by creating longer and longer periods which will result in a chaotic

solution. The frequency spectrum is more densely filled. A complete study of the chaotic nature of this solution could be performed by computing the Lyapunov spectrum or a more involved stability analysis of the torus solution. This point is however not the scope of the present study which is focused on the appearance of quasiperiodic solutions and their link to Frequency combs in MEMs dynamics.

5 Conclusion and further developments

In this paper we have developed analytical results for 1:2 internally resonant coupled oscillators. Even though this analysis is classical in nonlinear vibration theory, new insights have been reported, in particular with regard to the identification of the two backbones and their corresponding parabolic mode shapes and the analytical derivation of the NS boundary curves. All these results have been also put under the frame of explaining the appearance of FC in MEMs dynamics, a subject that give rise to numerous investigations in the recent years, and all the results have been applied to a MEMS arch structure in order to underline the predictive capacity of the analytical NS boundary curve. This result can be helpful in a context of MEMs design for accurate and fast predictions since the QP solutions are sometimes intentionally searched for.

Starting from the normal form of the dynamical system we inspected the conservative solution providing a clear identification of the mode shapes and solution branches. By extending our study to the forced and damped condition we were able to retrieve a closed form solution for the NS boundary curve. We inspected in depth the behaviour of the bifurcation boundary by varying the system parameters and comparing it with the conservative and the non-conservative solutions. We proved the validity of our findings in the challenging simulation of a MEMS structure example. The analytical solution has been validated against several numerical methods including numerical continuation procedures (MANLAB), reduced order models solved with direct time integration or the Harmonic Balance Method and eventually also with full FEM approaches.
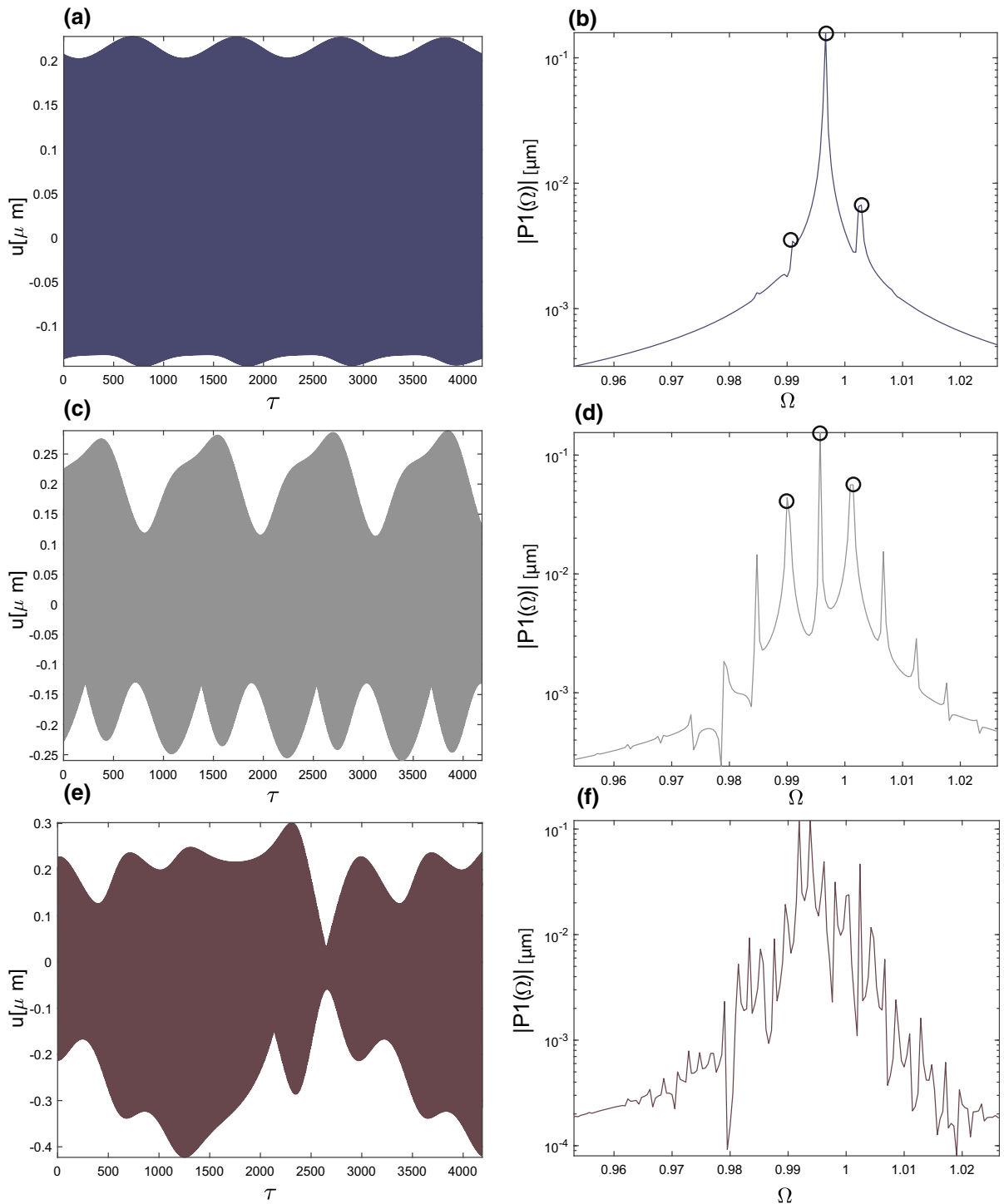
Fig. 20 Time histories (left column) and corresponding Frequency spectrum (right column) obtained by direct time integration of the full FE model, following the branch of QP solution by order of decreasing frequencies. First line: $\Omega = 0.9965$, birth of the QP solution. Second and third lines: $\Omega = 0.9956$ and 0.9939
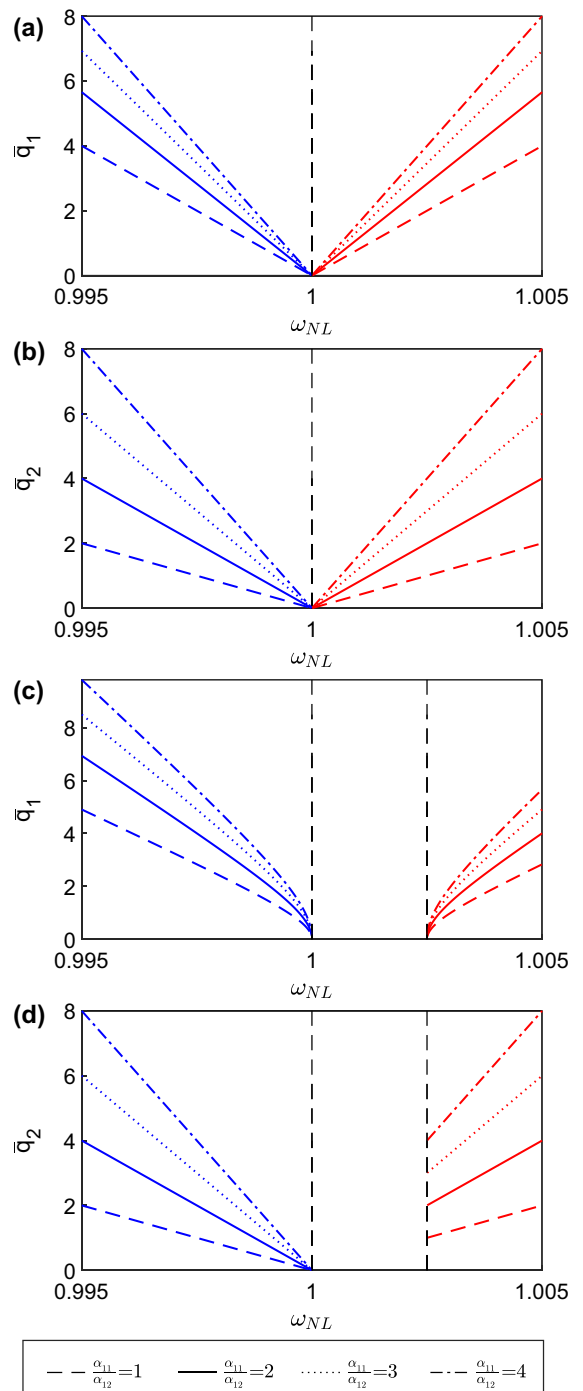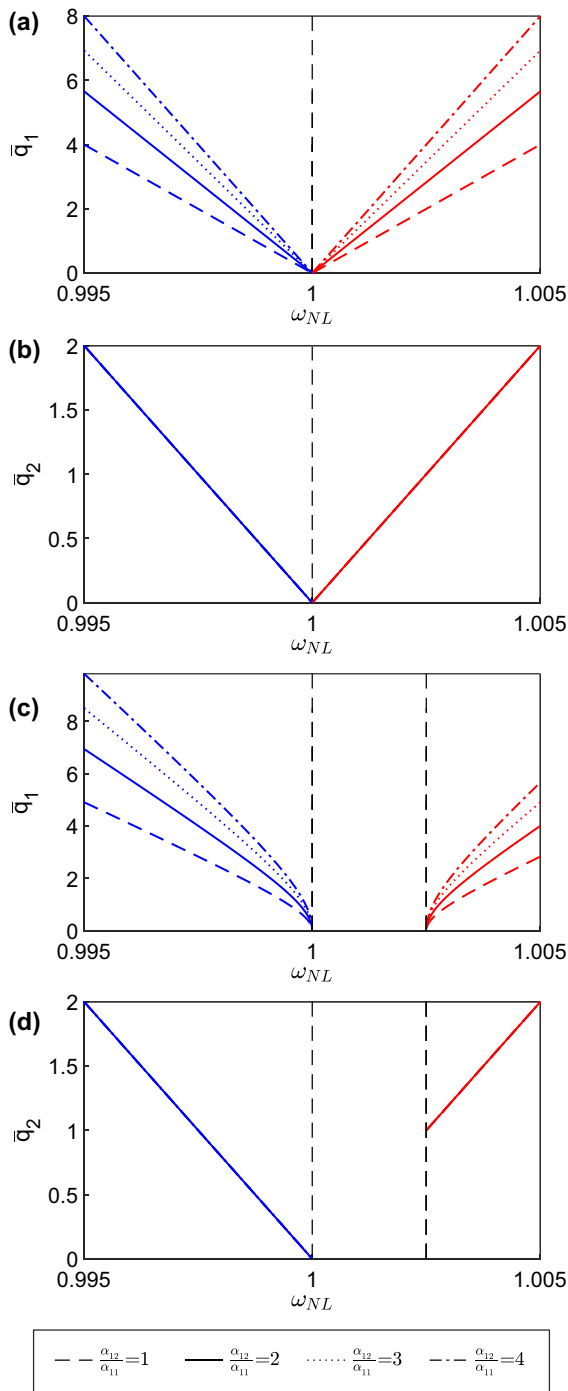
Fig. 21 Behaviour of the backbones when α_{12}/α_{11} is changed keeping fixed $\alpha_{12} = 1 \cdot 10^{-2}$. In these plots the line color marks with blue the p^- and with red the p^+ mode, the black dashed line marks $\Omega = \omega_2/2$. Figure a) and b) represent the backbone $\bar{q}_1$ and $\bar{q}_2$ respectively when $\omega_2 - 2\omega_1 = 0$. Figure c) and d) represent the backbone $\bar{q}_1$ and $\bar{q}_2$ respectively when $\omega_2 - 2\omega_1 = 5 \cdot 10^{-3}$

Fig. 22 Behaviour of the backbones when α_{11}/α_{12} is changed keeping fixed $\alpha_{11} = 1 \cdot 10^{-2}$. In these plots the line color marks with blue the p^- and with red the p^+ mode, the black dashed line marks $\Omega = \omega_2/2$. Figure a) and b) represent the backbone $\bar{q}_1$ and $\bar{q}_2$ respectively when $\omega_2 - 2\omega_1 = 0$. Figure c) and d) represent the backbone $\bar{q}_2$ and $\bar{q}_2$ respectively when $\omega_2 - 2\omega_1 = 5 \cdot 10^{-3}$

A good agreement between the analytical results and the numerical approach is always observed. In particular, the NS boundary provides a nearly perfect prediction of the quasi-periodic regime arising and a very good estimate of the incommensurate frequency. The formulas proposed prove useful for design applications on real devices and structures. The closed form solution allows exploring in depth the resonance phenomena with low computational effort. Further development are currently undertaken in order to reframe the cases of 1:1 and 1:3 internal resonance within the same analyses, underlining the existence of different families of periodic orbits , deriving accurate predictive solutions for the NS boundary curve, in order to shed new light and unify analyses of the emergence of QP solutions in nonlinear oscillators with applications to MEMs dynamics.

Declarations

Conflict of interest The authors declare that they have no conflict of interest.

Fig. 23 The figures show the NS boundary behaviour corresponding to $\omega_1 = 1$, $\omega_2 = 2.005$, $\mu_1 = \mu_2 = 1.5 \cdot 10^{-3}$ for different ratio α_{12}/α_{11} keeping $\alpha_{12} = 5 \cdot 10^{-2}$

Appendix

1. General nonlinear coefficients in Eq. 1

This section shows how the formulas proposed in the paper can be used into the general case of uncorrelated α_{12} and α_{11}. We will mainly focus on the effect of a different sets of nonlinear coefficients on backbones and NS boundary. Considering the backbone curves, keeping the frequency detuning $\omega_2 - 2\omega_1$ fixed and varying the non-linear coefficients α_{12} and α_{11} ratios, the results are shown in Figs. 21 and 22.
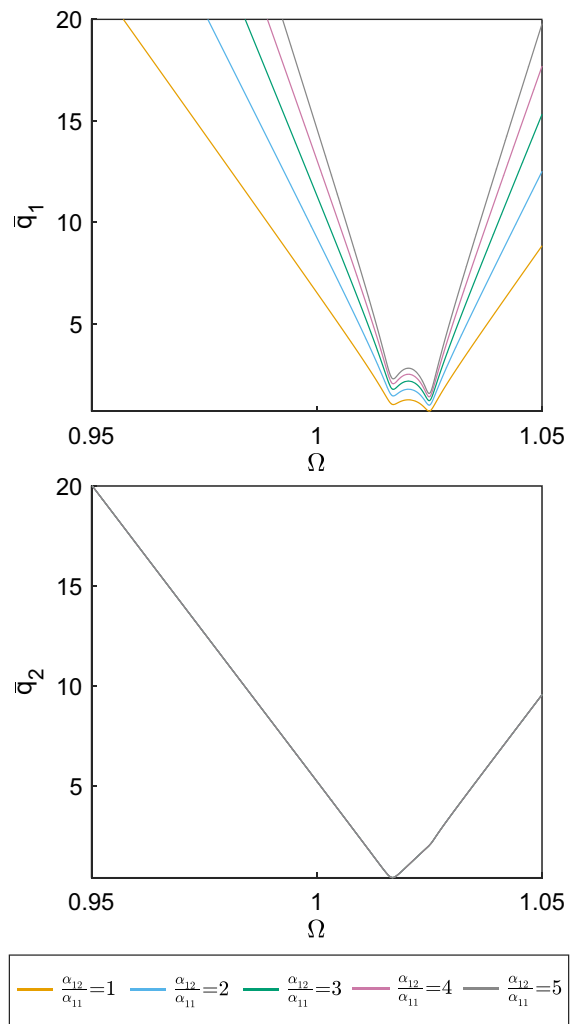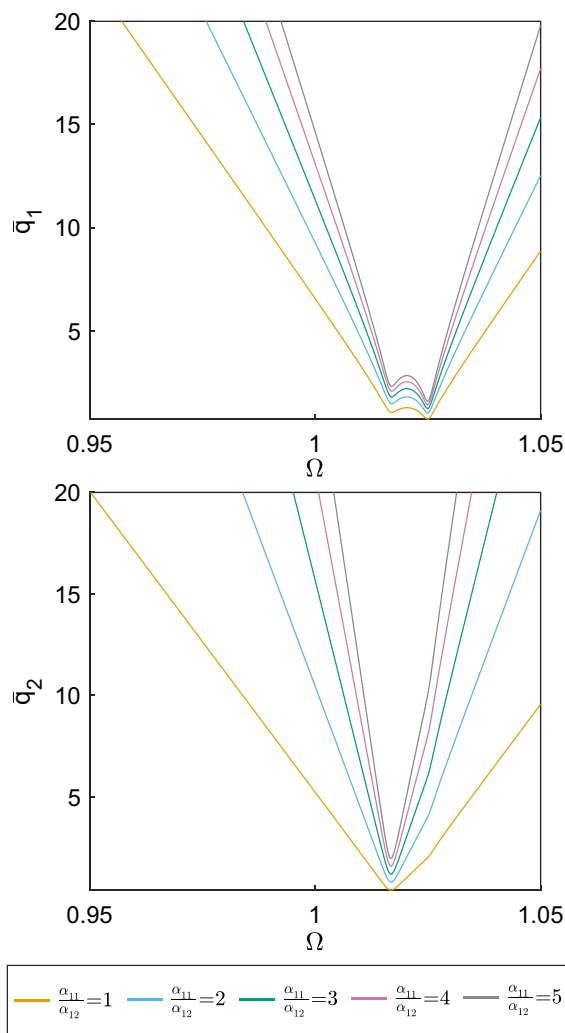
Fig. 24 The figures show the NS boundary behaviour corresponding to $\omega_1 = 1$, $\omega_2 = 2.005$, $\mu_1 = \mu_2 = 1.5 \cdot 10^{-3}$ for different ratio α_{11}/α_{12} keeping $\alpha_{11} = 5 \cdot 10^{-2}$

Fig. 21 assumes $\alpha_{12} = 1 \cdot 10^{-2}$ and it considers different values of the ratio α_{12}/α_{11}. Figure 21 a) and b) refer to a detuning value $\sigma_1 = 0$, while Fig. 21c) and d) refer to $\sigma_1 = 5 \cdot 10^{-3}$. The backbones of the second oscillator response is invariant with respect to the ratio α_{12}/α_{11}. This is reasonable because only α_{12} appears in Eq. (16a). The $\bar{q}_1$ backbone tends to grow with the ratio α_{12}/α_{11} preserving the same shape . The σ_1 value introduces a curvature in the $\bar{q}_1$ mode response and left unchanged the starting point of the $\bar{q}_2$ backbone.

Fig. 22 assumes $\alpha_{11} = 1 \cdot 10^{-2}$ and considers different values of the ratio α_{11}/α_{12}. Fig. 22 a) and b)

refer to $\sigma_1 = 0$, while Fig. 22c) and d) to $\sigma_1 = 5 \cdot 10^{-3}$. The backbone of both oscillators grow with the ratio α_{11}/α_{12} preserving their shape. The σ_1 value introduces a curvature in the $\bar{q}_1$ mode response and shifts to higher amplitudes the starting point of the $\bar{q}_2$ backbone.

We now inspect the NS boundary behaviour. We consider the system parameters $\omega_1 = 1$, $\omega_2 = 2.005$, $\mu_1 = \mu_2 = 1.5 \cdot 10^{-3}$ and we plot in Fig. 23 the NS boundaries corresponding to different ratio α_{12}/α_{11}, keeping $\alpha_{12} = 5 \cdot 10^{-2}$. The plots show that in the $\bar{q}_1$ amplitude the NS boundary tends to enlarge with a lower ratio (higher α_{11}) while it is identical in the $\bar{q}_2$ response. This is reasonable because only α_{12} appears in Eq. (33). Considering the same system, in Fig. 24 the NS boundaries for different ratio α_{11}/α_{12}, keeping $\alpha_{11} = 5 \cdot 10^{-2}$ are plotted. The plots show that in both the amplitudes the NS boundary tends to enlarge with lower ratio (higher α_{12}).

2. Conservative system

This section presents the details of the MS solution in Sect. 2.1 for the conservative case, i.e. with no forcing and damping. We insert the MS approximation $q_i(t) = q_{i0}(T_0, T_1) + \varepsilon q_{i1}(T_0, T_1)$ into Eq. (1) and split the resulting terms using ε as sorting parameter. Consequently, we get a first order system:

$$\begin{aligned} D_0^2 q_{10} + \omega_1^2 q_{10} = 0, \\ D_0^2 q_{20} + \omega_2^2 q_{20} = 0, \end{aligned} \tag{37}$$

and a second order system:

$$\begin{aligned} D_0^2 q_{11} + \omega_1^2 q_{11} = -2D_0 D_1 q_{10} + \bar{\alpha}_{12} q_{10} q_{20}, \\ D_0^2 q_{12} + \omega_2^2 q_{12} = -2D_0 D_1 q_{20} + \bar{\alpha}_{11} q_{10}^2, \end{aligned} \tag{38}$$

in which D_i^k denotes the order k derivative with respect to the time scale $i = 0, 1$. Eq. (37) describes two linear uncoupled oscillators with motion given by:

$$q_{11} = A_1 e^{\mathbb{i}\omega_1 T_0} + \bar{A}_1 e^{-\mathbb{i}\omega_1 T_0} \tag{39a}$$

$$q_{21} = A_2 e^{\mathbb{i}\omega_2 T_0} + \bar{A}_2 e^{-\mathbb{i}\omega_2 T_0} \tag{39b}$$

Inserting the solution of Eq. (37) in Eq. (38) we get an expression with A_i as unknowns. Nullifying secular terms we get the conditions:

$$\bar{\alpha}_{12}A_2\bar{A}_1 e^{\mathring{\imath}T_1\sigma_1} + 2\mathring{\imath}\omega_1 A_1' = 0, \tag{40a}$$

$$A_1^2 \bar{\alpha}_{11} + 2\mathring{\imath}\omega_2 A_2' e^{\mathring{\imath}T_1\sigma_1} = 0. \tag{40b}$$

To solve Eq. (40) we need to expand A_i in polar form as $A_i(T_1) = \frac{1}{2}a_i(T_1)\exp\left(\mathring{\imath}\theta_i(T_1)\right)$, $i = 1, 2$. Insert A_i in Eq. (40) and imposing that the real and imaginary part vanish independently, we get Eq. (4).

As required by the stability analysis in Sect. 2.3 we finally compute the Jacobian matrix of system. (7), i.e.:

$$J = \begin{pmatrix} J_{11} & 0 & J_{13} & J_{14} \\ 0 & 0 & J_{23} & J_{24} \\ J_{31} & 0 & 0 & J_{34} \\ J_{41} & 0 & J_{43} & J_{44} \end{pmatrix}, \tag{41}$$

with:

$$J_{11} = \frac{\bar{\alpha}_{12}a_2\sin(\gamma_p)}{4\omega_1}, \quad J_{13} = \frac{\bar{\alpha}_{12}a_1\sin(\gamma_p)}{4\omega_1},$$

$$J_{14} = \frac{\bar{\alpha}_{12}a_1a_2\cos(\gamma_p)}{4\omega_1}, \quad J_{23} = \frac{\bar{\alpha}_{12}\cos(\gamma_p)}{4\omega_1},$$

$$J_{24} = -\frac{\bar{\alpha}_{12}a_2\sin(\gamma_p)}{4\omega_1}, \quad J_{31} = -\frac{\bar{\alpha}_{11}a_1\sin(\gamma_p)}{2\omega_2},$$

$$J_{34} = -\frac{\bar{\alpha}_{11}a_1^2\cos(\gamma_p)}{4\omega_2}, \quad J_{41} = -\frac{\bar{\alpha}_{11}a_1\cos(\gamma_p)}{2a_2\omega_2},$$

$$J_{43} = \frac{1}{2}\cos(\gamma_p)\left(\frac{\bar{\alpha}_{12}}{\omega_1} + \frac{\bar{\alpha}_{11}a_1^2}{2a_2^2\omega_2}\right)$$

$$J_{44} = -\frac{\sin(\gamma_p)}{4a_2}\left(\frac{2\bar{\alpha}_{12}a_2^2}{\omega_1} - \frac{\bar{\alpha}_{11}a_1^2}{\omega_2}\right).$$

3. Forced and damped system

Starting from Eq. (1) we sort the non-linearities using a book-keeping parameter ε. We assume a first order approximation, thus we rewrite Eq. (1) in the form:

$$\ddot{q}_1 + \omega_1^2 q_1 = \varepsilon[-2\bar{\mu}_1\dot{q}_1 - \bar{\alpha}_{12}q_1q_2 + \bar{F}\cos(\Omega t)], \tag{42a}$$

$$\ddot{q}_2 + \omega_2^2 q_2 = \varepsilon[-2\bar{\mu}_2\dot{q}_2 - \bar{\alpha}_{11}q_1^2]. \tag{42b}$$

The external forcing angular frequency is related to the eigenfrequency through Eq. (23). Proceeding as for the conservative case (see from Eq. (38) to Eq. (40)), we get the solvability condition:

$$\bar{\alpha}_{12}A_2\bar{A}_1 e^{\mathring{\imath}T_1\sigma_1} + 2\mathring{\imath}\omega_1\left(A_1\bar{\mu}_1 + A_1'\right) - \frac{1}{2}\bar{F}e^{\mathring{\imath}T_1\sigma_2} = 0, \tag{43a}$$

$$A_1^2\bar{\alpha}_{11} + 2\mathring{\imath}e^{\mathring{\imath}T_1\sigma_1}\omega_2\left(A_2\bar{\mu}_2 + A_2'\right) = 0. \tag{43b}$$

Inserting the polar form of A_i, $i = 1, 2$ (see Appendix 2) in Eq. (43) and imposing that the real and imaginary parts vanish, we get the system of four equations in Eq. (24).

Considering the A1-mode condition $a_1 \neq 0$ and $a_2 = 0$, Eq. (1) admit a nonzero solution for a_1 only if α_{11} is zero, but this is a degenerate condition. Thus, the A1-mode is not allowed.

Considering the A2-mode condition $a_2 \neq 0$ and $a_1 = 0$, Eq. (1) implies a zero forcing value, and consequently nonzero solutions exist only if the damping term also is zero. This is a degenerate condition since it is the one predicted by the conservative case, thus the A2-mode in damped and forced conditions is impossible.

The coupled solutions are obtained from Eq. (24), as detailed in Sect. 3, and are given by Eq. (26).

In order to address the stability of the coupled solutions derived in Sect. 3, one needs the Jacobian matrix for Eq. (26), i.e.:

$$J = \begin{pmatrix} J_{11} & J_{12} & J_{13} & J_{14} \\ J_{21} & J_{22} & J_{23} & J_{24} \\ J_{31} & 0 & J_{33} & J_{34} \\ J_{41} & J_{42} & J_{43} & J_{44} \end{pmatrix}, \tag{44}$$

with:

$$J_{11} = \frac{\bar{\alpha}_{12} a_2 \sin(\gamma_2) - 4\bar{\mu}_1 \omega_1}{4\omega_1},$$

$$J_{12} = -\frac{\bar{F}\cos(\gamma_1)}{2\omega_1},$$

$$J_{13} = \frac{\bar{\alpha}_{12} a_1 \sin(\gamma_2)}{4\omega_1}, J_{14} = \frac{\bar{\alpha}_{12} a_1 a_2 \cos(\gamma_2)}{4\omega_1},$$

$$J_{21} = \frac{\bar{F}\cos(\gamma_1)}{2a_1^2\omega_1},$$

$$J_{22} = \frac{\bar{F}\sin(\gamma_1)}{2a_1\omega_1},$$

$$J_{23} = \frac{\bar{\alpha}_{12}\cos(\gamma_2)}{4\omega_1},$$

$$J_{24} = -\frac{\bar{\alpha}_{12} a_2 \sin(\gamma_2)}{4\omega_1},$$

$$J_{31} = -\frac{\bar{\alpha}_{11} a_1 \sin(\gamma_2)}{2\omega_2},$$

$$J_{33} = -\bar{\mu}_2,$$

$$J_{34} = -\frac{\bar{\alpha}_{11} a_1^2 \cos(\gamma_2)}{4\omega_2},$$

$$J_{41} = \frac{\bar{F}\cos(\gamma_1)}{a_1^2\omega_1} - \frac{\bar{\alpha}_{11} a_1 \cos(\gamma_2)}{2a_2\omega_2},$$

$$J_{42} = \frac{\bar{F}\sin(\gamma_1)}{a_1\omega_1},$$

$$J_{43} = \frac{1}{4}\cos(\gamma_2)\left(\frac{2\bar{\alpha}_{12}}{\omega_1} + \frac{\bar{\alpha}_{11} a_1^2}{a_2^2\omega_2}\right)$$

$$J_{44} = -\frac{1}{2}\sin(\gamma_2)\left(\frac{\bar{\alpha}_{12} a_2}{\omega_1} - \frac{\bar{\alpha}_{11} a_1^2}{2a_2\omega_2}\right).$$

4. Coefficients of polynomials Eq. (29) and Eq. (33)

$$c_1 = 2(\mu_1 + \mu_2),$$

$$c_2 = \frac{a_2\alpha_{12}}{\omega_1}\sqrt{\mu_2^2 + (\omega_2 - 2\Omega)^2} - \frac{a_2^2\alpha_{12}^2}{16\omega_1^2}$$
$$+ \mu_1^2 + \mu_2^2 + 4\mu_1\mu_2 - 2\omega_1\Omega - 4\omega_2\Omega$$
$$+ \omega_1^2 + \omega_2^2 + 5\Omega^2,$$

$$c_3 = \frac{a_2\alpha_{12}}{\omega_1}(\mu_1 + \mu_2)\sqrt{\mu_2^2 + (\omega_2 - 2\Omega)^2}$$
$$- \frac{a_2^2\alpha_{12}^2\mu_2}{8\omega_1^2} + 2\mu_1\left(\mu_2^2 + (\omega_2 - 2\Omega)^2\right)$$
$$+ 2\mu_2(\Omega - \omega_1)^2 + 2\mu_2\mu_1^2,$$

$$c_4 = \frac{\sqrt{\mu_2^2 + (\omega_2 - 2\Omega)^2}}{16\omega_1^2}\left(3a_2^2\alpha_{12}^2\sqrt{\mu_2^2 + (\omega_2 - 2\Omega)^2}\right.$$
$$+ 16a_2\alpha_{12}\omega_1(\mu_1\mu_2 - (\Omega - \omega_1)(2\Omega - \omega_2))$$
$$\left. + 16\omega_1^2\left(\mu_1^2 + (\Omega - \omega_1)^2\right)\sqrt{\mu_2^2 + (\omega_2 - 2\Omega)^2}\right),$$
$$\tag{45}$$

$$b_1 = \frac{\alpha_{12}^4\mu_1\mu_2}{64\omega_1^4},$$

$$b_2 = -\frac{\alpha_{12}^3(\mu_1 + \mu_2)^2\sqrt{\mu_2^2 + (\omega_2 - 2\Omega)^2}}{8\omega_1^3},$$

$$b_3 = -\frac{\alpha_{12}^2}{2\omega_1^2}\mu_1\mu_2\cdot$$
$$\left(\mu_1^2 + \mu_2^2 + 2\mu_1\mu_2 - 2\omega_1\Omega + 4\omega_2\Omega + \omega_1^2 - \omega_2^2 - 3\Omega^2\right),$$

$$b_4 = \frac{2\alpha_{12}}{\omega_1}(\mu_1 + \mu_2)^2\sqrt{\mu_2^2 + (\omega_2 - 2\Omega)^2}\cdot$$
$$\left(\mu_1^2 + 2\mu_2\mu_1 + \mu_2^2 + (\omega_1 + \omega_2 - 3\Omega)^2\right),$$

$$b_5 = 4\left(\left(\mu_1\left(\mu_2^2 + (\omega_2 - 2\Omega)^2\right) + \mu_2(\Omega - \omega_1)^2 + \mu_2\mu_1^2\right)\cdot\right.$$
$$\left(\mu_1\left(4\mu_2^2 + (\Omega - \omega_1)^2\right) + \mu_2\left(\mu_2^2 + (\omega_2 - 2\Omega)^2\right)\right.$$
$$\left. + \mu_1^3 + 4\mu_2\mu_1^2\right) - (\mu_1 + \mu_2)^2\left(\mu_1^2 + (\Omega - \omega_1)^2\right)$$
$$\left.\left(\mu_2^2 + (\omega_2 - 2\Omega)^2\right)\right).$$
$$\tag{46}$$

5. Asymptotic analysis of the extrema of the NS boundary curve

In order to search for the extrema of the NS boundary curve, we compute the derivative of Eq. (33), defining the NS boundary, with respect to the external forcing frequency Ω:

$$d_1(\Omega)\bar{q}_2^3 + d_2(\Omega)\bar{q}_2^2 + d_3(\Omega)\bar{q}_2 + d_4(\Omega) = 0, \qquad (47)$$

where the explicit expressions for all the coefficients read:

$$d_1 = -\frac{\alpha_{12}^3(\mu_1+\mu_2)^2(2\Omega-\omega_2)}{4\omega_1^3\sqrt{\mu_2^2+(\omega_2-2\Omega)^2}},$$

$$d_2 = \frac{\alpha_{12}^2\mu_1\mu_2(\omega_1-2\omega_2+3\Omega)}{\omega_1^2},$$

$$\begin{aligned}
d_3 = &\frac{4\alpha_{12}}{\omega_1\sqrt{\mu_2^2+(\omega_2-2\Omega)^2}}\Bigg((\mu_1+\mu_2)^2\bigg(\mu_1^2(2\Omega-\omega_2)\\
&+2\mu_2\mu_1(2\Omega-\omega_2)+\mu_2^2(-3\omega_1-4\omega_2+11\Omega)\\
&+(2\Omega-\omega_2)\Big(-21\omega_2\Omega+\omega_1(5\omega_2-12\Omega)\\
&+\omega_1^2+4\omega_2^2+27\Omega^2\Big)\bigg)\Bigg),
\end{aligned}$$

$$\begin{aligned}
d_4 = &16\mu_1\mu_2\Bigg(\mu_1^2(-\omega_1-2\omega_2+5\Omega)\\
&+\mu_2^2(-\omega_1-2\omega_2+5\Omega)+2\mu_1\mu_2(-\omega_1-2\omega_2+5\Omega)\\
&+9\omega_1\Omega^2-18\omega_2\Omega^2-\omega_1^2\Omega+11\omega_2^2\Omega-8\omega_1\omega_2\Omega\\
&-\omega_1^3-2\omega_2^3+\omega_1\omega_2^2+2\omega_1^2\omega_2+9\Omega^3\Bigg).
\end{aligned}$$

$$(48)$$

Due to the complexity of the expressions, a numerical solution is mandatory in general. However, in specific cases one can get an analytical estimate for the extrema. First, we simplify Eq. (47) considering $\mu_1 = \mu_2 = \mu$ and by sorting it with respect to μ we get:

$$\frac{(g_1\mu^4+g_2\mu^2)}{\omega_1^3\sqrt{\mu^2+(2\Omega-\omega_2)^2}} + g_3\mu^2 = 0, \qquad (49)$$

with

$$\begin{aligned}
g_1 = &272\alpha_{12}\bar{q}_2\omega_1^2\Omega-48\alpha_{12}\bar{q}_2\omega_1^3-112\alpha_{12}\bar{q}_2\omega_2\omega_1^2\\
&-64\omega_1^4\sqrt{\mu^2+(2\Omega-\omega_2)^2}+320\omega_1^3\Omega\sqrt{\mu^2+(2\Omega-\omega_2)^2}\\
&-128\omega_2\omega_1^3\sqrt{\mu^2+(2\Omega-\omega_2)^2},
\end{aligned}$$

$$\begin{aligned}
g_2 = &864\alpha_{12}\bar{q}_2\omega_1^2\Omega^3-384\alpha_{12}\bar{q}_2\omega_1^3\Omega^2-1104\alpha_{12}\bar{q}_2\omega_2\omega_1^2\Omega^2\\
&+32\alpha_{12}\bar{q}_2\omega_1^4\Omega+352\alpha_{12}a_2\omega_2\omega_1^3\Omega\\
&+464\alpha_{12}\bar{q}_2\omega_2^2\omega_1^2\Omega-16\alpha_{12}\bar{q}_2\omega_2\omega_1^4-80\alpha_{12}\bar{q}_2\omega_2^2\omega_1^3\\
&-64\alpha_{12}\bar{q}_2\omega_2^3\omega_1^2+\alpha_{12}^3\bar{q}_2^3\omega_2-2\alpha_{12}^3\bar{q}_2^3\Omega,
\end{aligned}$$

$$\begin{aligned}
g_3 = &3\alpha_{12}^2\bar{q}_2^2\omega_1\Omega+\alpha_{12}^2\bar{q}_2^2\omega_1^2-2\alpha_{12}^2\bar{q}_2^2\omega_2\omega_1\\
&+144\omega_1^3\Omega^3+144\omega_1^4\Omega^2-288\omega_2\omega_1^3\Omega^2\\
&-16\omega_1^5\Omega-128\omega_2\omega_1^4\Omega+176\omega_2^2\omega_1^3\Omega\\
&-16\omega_1^6+32\omega_2\omega_1^5+16\omega_2^2\omega_1^4-32\omega_2^3\omega_1^3.
\end{aligned}$$

$$(50)$$

Inserting $\Omega = \omega_2/2$ in Eq. (50) we remark that g_2, the leading term in μ, vanishes. Thus $\Omega = \omega_2/2$ is an asymptotical extrema for the problem and corresponds to a minimum.

We next consider the limit $\mu \to 0$. The leading order term is proportional to μ^2 and is given by:

$$\frac{g_2}{\omega_1^3\sqrt{(2\Omega-\omega_2)^2}} + g_3 = 0. \qquad (51)$$

This expression is the asymptotic approximation of Eq. (47) and it can be be expressed in the same form as Eq. (47), with:

$$d_1 = -\frac{\alpha_{12}^3}{\omega_1^3},$$

$$d_2 = \frac{\alpha_{12}^2(\omega_1-2\omega_2+3\Omega)}{\omega_1^2},$$

$$d_3 = \frac{16\alpha_{12}}{\omega_1}\left(-21\omega_2\Omega+\omega_1(5\omega_2-12\Omega)+\omega_1^2+4\omega_2^2+27\Omega^2\right),$$

$$\begin{aligned}
d_4 = &-16\Bigg(18\omega_2\Omega^2-\omega_1\left(-8\omega_2\Omega+\omega_2^2+9\Omega^2\right)\\
&-11\omega_2^2\Omega+\omega_1^2(\Omega-2\omega_2)+\omega_1^3+2\omega_2^3-9\Omega^3\Bigg).
\end{aligned}$$

$$(52)$$

Eq. (51) can be directly solved with respect to Ω if we consider that the NS boundary tends to approach zero when the damping tends to zero. With this assumption, only the lower order terms with respect to $\bar{q}_2$, i.e. d_4

and d_3, are relevant. This provides a linearised version of the NS minima problem and has the solution $\Omega = (\omega_2 + \omega_1)/3$ independent of its amplitude.

References

1. Awrejcewicz J (1990) Bifurcation portrait of the human vocal cord oscillations. J Sound Vibr 136(1):151–156
2. Awrejcewicz J (1990) Numerical investigations of the constant and periodic motions of the human vocal cords including stability and bifurcation phenomena. Dyn Stab Syst 5(1):11–28
3. Awrejcewicz J, Reinhardt WD (1990) Quasiperiodicity, strange non-chaotic and chaotic attractors in a forced two degrees-of-freedom system. Zeitschrift für angewandte Mathematik und Physik ZAMP 41(5):713–727
4. Awrejcewicz J, Reinhardt WD (1990) Some comments about quasi-periodic attractors. J Sound Vibr 139(2): 347–350
5. Cenedese M, Haller G (2020) How do conservative backbone curves perturb into forced responses? a Melnikov function analysis. Proc Royal Soc A 476(2234):20190494
6. Clementi F, Lenci S, Rega G (2020) 1: 1 internal resonance in a two dof complete system: a comprehensive analysis and its possible exploitation for design. Meccanica 55: 1309–1332
7. Czaplewski DA, Chen C, Lopez D, Shoshani O, Eriksson AM, Strachan S, Shaw SW (2018) Bifurcation generated mechanical frequency comb. Phys Rev Lett 121(24):244302
8. Czaplewski DA, Strachan S, Shoshani O, Shaw SW, López D (2019) Bifurcation diagram and dynamic response of a mems resonator with a 1: 3 internal resonance. Appl Phys Lett 114(25):254104
9. Dauxois T, Ruffo S, Torcini A (1998) Analytical estimation of the maximal Lyapunov exponent in oscillator chains. J Phys IV France 08(PR6):147–156
10. Del'Haye P, Schliesser A, Arcizet O, Wilken T, Holzwarth R, Kippenberg TJ (2007) Optical frequency comb generation from a monolithic microresonator. Nature 450(7173): 1214–1217
11. Detroux T, Renson L, Masset L, Kerschen G (2015) The harmonic balance method for bifurcation analysis of large-scale nonlinear mechanical systems. Comput Methods Appl Mech Eng 296:18–38
12. Frangi A, De Masi B, Confalonieri F, Zerbini S (2015) Threshold shock sensor based on a bistable mechanism: design, modeling, and measurements. J Microelectromech Syst 24(6):2019–2026
13. Frangi A, Gobat G (2019) Reduced order modelling of the non-linear stiffness in mems resonators. Int J Non-Linear Mech 116:211–218
14. Ganesan A, Do C, Seshia A (2017) Frequency transitions in phononic four-wave mixing. Appl Phys Lett 111(6):064101
15. Ganesan A, Do C, Seshia A (2017) Phononic frequency comb via intrinsic three-wave mixing. Phys Rev Lett 118(3):033903
16. Ganesan A, Do C, Seshia A (2018) Phononic frequency comb via three-mode parametric resonance. Appl Phys Lett 112(2):021906
17. Givois A, Tan JJ, Touzé C, Thomas O (2020) Backbone curves of coupled cubic oscillators in one-to-one internal resonance: bifurcation scenario, measurements and parameter identification. Meccanica 55:481–503
18. Guckenheimer J, Holmes P (2013) Nonlinear oscillations, dynamical systems, and bifurcations of vector fields, vol 42. Springer Science & Business Media
19. Guerrieri A, Frangi A, Falorni L (2018) An investigation on the effects of contact in mems oscillators. J Microelectromech Syst 27(6):963–972
20. Guillot L, Cochelin B, Vergez C (2019) A taylor series-based continuation method for solutions of dynamical systems. Nonlinear Dyn 98(4):2827–2845
21. Guillot L, Vigué P, Vergez C, Cochelin B (2017) Continuation of quasi-periodic solutions with two-frequency harmonic balance method. J Sound Vibr 394:434–450
22. Hajjaj A, Alfosail F, Younis MI (2018) Two-to-one internal resonance of mems arch resonators. Int J Non-Linear Mech 107:64–72
23. Hajjaj A, Jaber N, Hafiz MAA, Ilyas S, Younis MI (2018) Multiple internal resonances in mems arch resonators. Phys Lett A 382(47):3393–3398
24. Haragus M, Iooss G (2010) Local bifurcations, center manifolds, and normal forms in infinite-dimensional dynamical systems. Springer, Dodrecht
25. Hollkamp JJ, Gordon RW (2008) Reduced-order models for non-linear response prediction: implicit condensation and expansion. J Sound Vibr 318:1139–1153
26. Kuznetsov YA (2013) Elements of applied bifurcation theory, vol 112. Springer, Dodrecht
27. Lenci S, Clementi F, Kloda L, Warminski J, Rega G (2020) Longitudinal-transversal internal resonances in Timoshenko beams with an axial elastic boundary condition. Nonlinear Dyn 103:3489–3513
28. Li TY, Yorke JA (2004) Period three implies chaos. The theory of chaotic attractors. Springer, Dodrecht, pp 77–84
29. Liang W, Eliyahu D, Ilchenko VS, Savchenkov AA, Matsko AB, Seidel D, Maleki L (2015) High spectral purity Kerr frequency comb radio frequency photonic oscillator. Nature Commun 6(1):1–8
30. Luongo A, Piccardo G (1998) Non-linear galloping of sagged cables in 1: 2 internal resonance. J Sound Vibr 214(5):915–940
31. Mahboob I, Dupuy R, Nishiguchi K, Fujiwara A, Yamaguchi H (2016) Hopf and period-doubling bifurcations in an electromechanical resonator. Appl Phys Lett 109(7): 073101
32. Manevitch AI, Manevitch LI (2003) Free oscillations in conservative and dissipative symmetric cubic two-degree-of-freedom systems with closed natural frequencies. Meccanica 38(3):335–348
33. Manneville P (1995) Dissipative structures and weak turbulence. Chaos-the interplay between stochastic and deterministic behaviour. Springer, Dodrecht, pp 257–272
34. Mielke A (2006) Hamiltonian and Lagrangian flows on center manifolds: with applications to elliptic variational problems. Springer, Dodrecht

35. Miles JW (1984) Resonantly forced motion of two quadratically coupled oscillators. Phys D 13:247–260

36. Monteil M, Touzé C, Thomas O, Benacchio S (2014) Nonlinear forced vibrations of thin structures with tuned eigenfrequencies: the cases of 1: 2: 4 and 1: 2: 2 internal resonances. Nonlinear Dyn 75(1–2):175–200

37. Nayfeh AH (2000) Nonlinear interactions: analytical, computational and experimental methods. Wiley, New-York

38. Nayfeh AH, Balachandran B (1989) Modal interactions in dynamical and structural systems. ASME Appl Mech Rev 42(11):175–201

39. Nayfeh AH, Balachandran B (2008) Applied nonlinear dynamics: analytical, computational, and experimental methods. Wiley, New Jersey

40. Nayfeh AH, Mook DT (1979) Nonlinear Oscill. Wiley, New Jersey

41. Neimark J (1959) On some cases of periodic motions depending on parameters. Dokl. Akad. Nauk SSSR 129: 736–739

42. Newhouse S, Ruelle D, Takens F (1978) Occurrence of strange axiom a attractors near quasi periodic flows on t m, m ≥ 3. Commun Math Phys 64(1):35–40

43. Opreni A, Boni N, Carminati R, Frangi A (2021) Analysis of the nonlinear response of piezo-micromirrors with the harmonic balance method. In: Actuators, vol. 10, p. 21. Multidisciplinary Digital Publishing Institute

44. Ouakad HM, Younis MI (2010) The dynamic behavior of MEMS arch resonators actuated electrically. Int J Non-Linear Mech 45(7):704–713

45. Park M, Ansari A (2019) Formation, evolution, and tuning of frequency combs in microelectromechanical resonators. J Microelectromech Syst 28(3):429–431

46. Ruzziconi L, Jaber N, Kosuru L, Bellaredj ML, Younis MI (2021) Experimental and theoretical investigation of the 2: 1 internal resonance in the higher-order modes of a MEMS microbeam at elevated excitations. J Sound Vibr 499: 115983

47. Ruzziconi L, Jaber N, Kosuru L, Bellaredj ML, Younis MI (2021) Two-to-one internal resonance in the higher-order modes of a MEMS beam: experimental investigation and theoretical analysis via local stability theory. Int J Non-Linear Mech 129:103664

48. Sacker RJ (2009) On invariant surfaces and bifurcation of periodic solutions of ordinary differential equations: Chapter ii: Bifurcation-mapping method. J Diff Equ Appl 15(8–9):759–774

49. Sharpe WN, Yuan B, Vaidyanathan R, Edwards RL (1997) Measurements of young's modulus, poisson's ratio, and tensile strength of polysilicon. In: Proceedings IEEE the tenth annual international workshop on micro electro mechanical systems. An investigation of micro structures, sensors, actuators, machines and robots, pp. 424–429. IEEE

50. Shen Y, Béreux N, Frangi A, Touzé C (2021) Reduced order models for geometrically nonlinear structures: assessment of implicit condensation in comparison with invariant manifold approach. Eur J Mech-A/Solids 86:104165

51. Strogatz SH (2018) Nonlinear dynamics and chaos with student solutions manual: With applications to physics, biology, chemistry, and engineering. CRC Press, London

52. Temam R (1990) Inertial manifolds. Math Intell 12(4): 68–74

53. Thomas O, Touzé C, Chaigne A (2005) Non-linear vibrations of free-edge thin spherical shells: modal interaction rules and 1: 1: 2 internal resonance. Int J Solids Struct 42(11–12):3339–3373

54. Thomsen JJ (2003) Vibrations and stability: advanced theory, analysis, and tools. Springer, London

55. Tien WM, Namachchivaya NS, Bajaj AK (1994) Non-linear dynamics of a shallow arch under periodic excitation–i. 1: 2 internal resonance. Int J Non-Linear Mech 29(3):349–366

56. Tien WM, Namachchivaya NS, Malhotra N (1994) Non-linear dynamics of a shallow arch under periodic excitation–ii. 1: 1 internal resonance. Int J Non-Linear Mech 29(3): 367–386

57. Touzé C, Amabili M (2006) Non-linear normal modes for damped geometrically non-linear systems: application to reduced-order modeling of harmonically forced structures. J Sound Vibr 298(4–5):958–981

58. Touzé C, Bilbao S, Cadot O (2012) Transition scenario to turbulence in thin vibrating plates. J Sound Vibr 331(2): 412–433

59. Touzé C, Thomas O, Amabili M (2011) Transition to chaotic vibrations for harmonically forced perfect and imperfect circular plates. Int J Non-linear Mech 46(1): 234–246

60. Udem T, Holzwarth R, Hänsch TW (2002) Optical frequency metrology. Nature 416(6877):233–237

61. Xie L, Baguet S, Prabel B, Dufour R (2016) Numerical tracking of limit points for direct parametric analysis in nonlinear rotordynamics. J Vibr Acoust 138(2):021007

62. Xie L, Baguet S, Prabel B, Dufour R (2017) Bifurcation tracking by harmonic balance method for performance tuning of nonlinear dynamical systems. Mech Syst Signal Process 88:445–461

63. Ye J, Cundiff ST (2005) Femtosecond optical frequency comb: principle, operation and applications. Springer, Dodrecht

64. Zakharov V, Ostrovsky L (2009) Modulation instability: the beginning. Phys D: Nonlinear Phenom 238(5):540–548